AUTONOMOUS DETECTION AND CHARACTERIZATION OF NUCLEAR MATERIALS USING CO-ROBOTS

A Thesis
Presented to
The Academic Faculty

by

Martin Zavala

In Partial Fulfillment
of the Requirements for the Degree
Nuclear and Radiological Engineering in the
School of Mechanical Engineering

Georgia Institute of Technology
May 2016

AUTONOMOUS DETECTION AND CHARACTERIZATION OF NUCLEAR MATERIALS USING CO-ROBOTS

Approval by:

Dr. Anna Erickson, Advisor
School of Mechanical Engineering
Georgia Institute of Technology

Dr. Jonathan Rogers
School of Mechanical Engineering
Georgia Institute of Technology

Dr. Chris Wang
School of Mechanical Engineering
Georgia Institute of Technology

Date Approved: 04/22/2016

ACKNOWLEDGEMENTS

I first and foremost wish to thank Dr. Anna Erickson, my thesis advisor for all of her help during my undergraduate and graduate career at Georgia Tech. She gave me a wonderful opportunity to work on such an innovative project and taught me immensely. I am grateful to my committee members, Dr. Jonathan Rogers and Dr. Chris Wang for their time and support. I would also like to thank Dr. Costello and his team, Dooroo Kim and Edward Sheuermann for their help understanding the robotics aspect of the project and Tyler Sisk for his help with the communication systems. Lastly in regards to the project, I would like to thank AREVA for funding my graduate program and their support throughout my graduate years at Tech.

In addition, I would like to thank the strong network of friends and family that have helped me strive. I would especially like to thank my parents Marie-Helene and Daniel, my sister Eleonor, my wonderful girlfriend Adele, and my amazing friends Gregory P., Colin, Greg S., Andrew, Wesley, Michael, and John. This thesis would not have been possible without the incredible company of all these people and many more that kept me motivated to further my studies.

I would like to dedicate this thesis to my paternal grandparents Huguette and Silvio Zavala who themselves pursued lives dedicated to research and pushed academia further. They inspired me to do the same and were amazing role-models, parents, and grandparents to my sister and me.

TABLE OF CONTENTS

LIST OF TABLES

LIST OF FIGURES

LIST OF SYMBOLS AND ABBREVIATIONS

NaI	Sodium Iodide
CZT	Cadmium Zinc Telluride
CsI(Tl)	Cesium Iodide, Thallium Activated
LaBr	Lanthanum Bromide
UAV	Unmanned Aerial Vehicles
GPS	Global Positional System
MeV	Megaelectron-Volt
keV	Kiloelectron-Volt
SiPM	Silicon Photomultiplier
APD	Avalanche Photodiode
RC	Remote Controlled
SPI	Serial Peripheral Interface
UART	Universal Asychronous Reciever / Transmitter
PWM	Pulse Width Modulation
NPM	Neutron Pulse Module

SUMMARY

Radiation safety is the biggest concern of the nuclear industry, and co-robots are a crucial component to insuring that safety. Currently, radiation mapping data is typically gathered using hand held detectors or other detection systems requiring constant human interaction. This results in direct exposure to radiation of the individual performing the survey. Co-robots can coordinate computer algorithms and human input to determine the most efficient and accurate methods of surveying these same regions while eliminating health hazards. These surveying methods can then be adapted for multiple uses in the industry including nonproliferation, maintenance, and accident response scenarios.

This work describes the process by which two vehicles were modified to detect radiation with minimal human interaction. An algorithm was developed to control the robot and to navigate the area of interest while ensuring that all sources are found. A compact detector system was used to keep the vehicles as small and light as possible. The vehicles were constructed to satisfy the requirements of the detector system and relay the necessary information back to the control station. The process, which is nearly fully autonomous, can map an area of interest and proceed to characterize the radiation materials that are found using neutron and gamma spectroscopy. The vehicles were tested in several scenarios which included obstacles, multiple sources, and shielding of the sources to determine the practicality of these co-robots. The evaluation of these co-robots was critical, as the future of radiation safety lies in the research and construction of small autonomous radiation detection systems to minimize the risk that radiation exposure poses to humans.

CHAPTER 1

INTRODUCTION

1.1 Motivation and Scope

Radiation mapping is the process of surveying a pre-determined area to acquire radiation levels and locate radiological sources. Currently, radiation mapping data is typically gathered using hand held detectors or detection systems requiring constant human interaction. The most common systems use Geiger-Müller tubes or ion chamber counters to manually observe and record counts. This results in direct irradiation of the individual performing the task. In addition, when a worker knowingly enters a high radiation zone, they must move quickly in order to limit exposure. Thus high radiation areas often cannot be precisely mapped due to dose constraints. The considered solution to this problem is to use autonomous vehicles to survey the area of interest.

Specifically, this approach has produced an algorithm for terrestrial, and eventually aerial vehicles to map the area of interest while locating the sources. By using a vehicle equipped with similar detector systems to current surveying systems, workers will not be subjected to radiation during the surveying process. The algorithms and detection systems used in this research were developed with the intention of eventually transitioning to aerial vehicles. Small multi-rotor robots are the ideal platform, as they are agile, easily adaptable, and can be controlled precisely and intuitively. Co-robots can also accrue much higher doses than humans and thus they can remain in dangerous areas for an extended period of time. The precision of mapping with these robots can be increased and applied using a closed loop, self-adjusting algorithm and control system. In addition, these multi-rotor vehicles have been an active area of research over the last decade. While terrestrial vehicles

may be hindered by obstacles or uneven terrain, they are still necessary to test a detection system and algorithm before upgrading to an aerial vehicle.

The recent incident at the Fukushima Daiichi plant best exemplifies the need for the proposed device. On March 11th 2011, a magnitude 9.0 earthquake hit Japan, followed by a devastating magnitude 9.1 tsunami [22]. The Fukushima Daiichi plant suffered major damage that destroyed all of the safety cooling mechanisms of the core, causing a meltdown. Workers were quickly evacuated from the plant and limited to 250 millisieverts of maximum allowable short term dose [7]. Accurate radiation maps were not readily available until several days after the catastrophe, when helicopters with lead shielding were flown at low altitudes, three kilometers from the site. The air dose rates collected over the 30 months can be seen in Figure 1.1 [5]. The maps improved during the months following the incident, but were not sufficiently accurate due to flight time constraints and the inability to remain in proximity to the plant. Even four years after the incident, there is still no radiation map of the immediate area surrounding the plant buildings. The proposed robot could have given an improved dose estimate more rapidly, and without any risk to workers. The vehicle could have also identified specific locations of containment radiation releases, which could have been crucial to further prevent contamination.

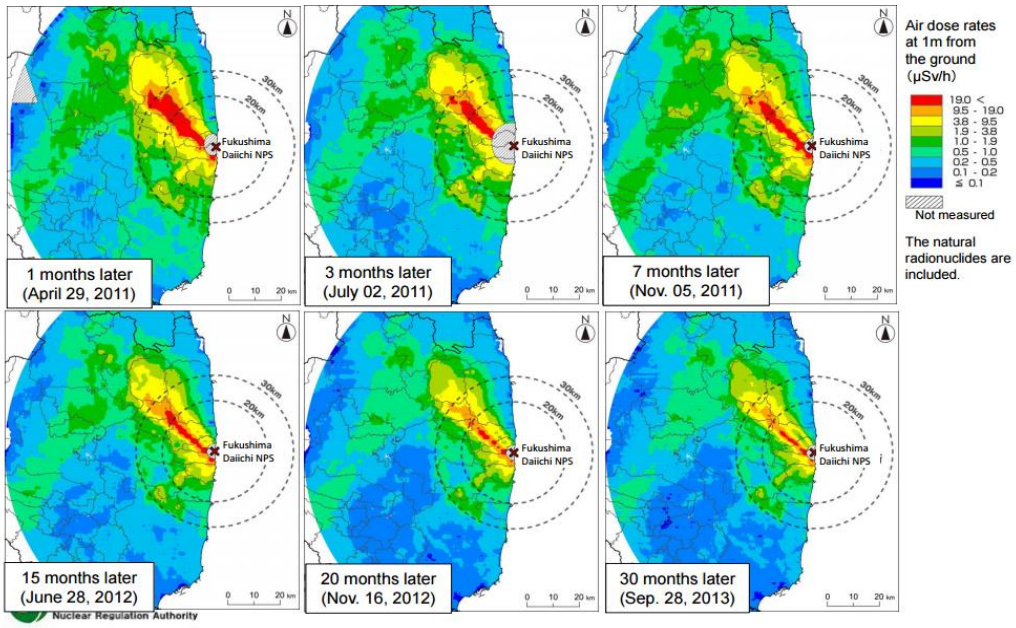

Figure 1.1: Air Dose Rates at Fukushima Daiichi Nuclear Power Plant using Aerial Detection provided by MEXT, [5]

Several ground robots were used at Fukushima in an attempt to infiltrate the collapsed buildings. The robots had varying levels of success. A few lost contact completely, while others were able to return crucial information.[7] Although the debris was not the only reason for their failures, an aerial vehicle with similar capabilities would not be impeded by those obstacles. The deployment of multi-rotor robots could also greatly improve the response time compared to current methods, but first a compact detection system for these vehicles must be tested.

Accident response scenarios such as Fukushima are only a small portion of the routines an autonomous/self-directed detection system could be used for. The portability and simplicity of the system make it well suited for other applications such as nonproliferation and monitoring. One strong motivator for these robots is the potential application against radiological threats. System mobility is crucial in finding malicious devices in an urban setting. The same robots can also be used for the monitoring of plants and other facilities to identify leaks or theft that may occur. Both of these currently require a multitude of well-placed sensors [11], whereas a robot can use one sensor to cover a much larger range and

pinpoint the material of interest if needed. A mobile vehicle can also offer an adaptable level of security based on the needs of the facility.

1.2 Thesis Outline

The remainder of this proposal will be presented in three sections, with supporting information appearing in the appendices. The first section will describe previous work in the fields of robotics and radiation mapping, followed by an introduction to the theory behind the work conducted. The subsequent section discusses the methodology of the work presented. The results section presents and analyses the findings using the aforementioned methodology. The final chapter outlines the conclusions from the work presented as well as future work to improve on the concept.

CHAPTER 2

BACKGROUND AND THEORY

2.1 Background

There are several important components to building the proposed system. The first component is the detector system. The detectors used by these vehicles are similar to those that radiation personnel would use for mapping. The biggest difference is the size of the system, which must be reduced significantly to fit these dynamic platforms. Several factors must be taken into account while choosing detector systems for these unmanned vehicles such as resolution, sensitivity, and the robustness of the detector. A wide range of detectors have been investigated regarding their possible application to similar projects. Some examples include CZT [13], CsI [17], and LaBr [20] detectors, or a combination of multiple detectors. [10][21] In this experiment, the primary detectors are gas filled detector tubes for neutron acquisition and inorganic scintillators for gamma acquisition. The detector system uses a boron lined gas detector for neutron detection. The cylindrical shape, with equal distribution of mass and light weight make the tube an ideal candidate for the detection system. The neutron tube is incorporated into the detection system for characterization of some heavier radiological elements such as uranium and plutonium for increased nonproliferation safety. The neutron detection can help identify sources based on the ratio of neutrons and photons emitted.

The gamma rays are counted using a cesium iodide, thallium (CsI(Tl)) activated, inorganic scintillator detector. CsI(Tl) is a particularly slow detector by inorganic scintillator standards, with a decay time between 0.7 and 3 micro seconds, as characterized by Valentine et al [23]. With longer decay times, the pulse pile up is more probable when higher activity sources produce more counts. The dead time, which occurs when surveying

larger activity sources, must be monitored closely to prevent diminished detector resolution. The CsI crystal provides many advantages, including a more robust crystal lattice and a comparatively larger gamma-ray absorption coefficient per unit size than other inorganic scintillators, such as NaI. [6] The relatively large 2-inch cubed crystal size is also remarkable for the sensitivity to lower activity sources. The CsI and B-10 detectors were combined into one detection system for the vehicle.

The objective in mapping an area is to explore the entire region, regardless of radiation levels, to get a complete representation of the radiation flux. Ideally, every grid point is measured once, but as obstacles are often encountered, Choset has developed the Boustrophedon cellular decomposition to bypass known obstacles. [1] Mapping algorithms using sensors such as those developed by Gonzalez-Banos et al., have also yielded accurate and timely results for mapping and exploring. [4] The previous work that best aligns with the proposed control systems was published by Cortez et al., which developed a hybrid control design. The design is a combination of a mapping area and detection method, which begins by surveying the area and devoting more time where the sources are thought to be present. [2] This concept was later expanded in 2009 with the addition of multiple robots. [3]

For the detection system to be effective, the vehicle must thoroughly explore and survey the area. There has been research produced on unmanned detection of radiation by many different vehicle configurations. The concept was presented as early as 1993 when H. Zafrir et al. proposed an unmanned airborne system for real time radiation monitoring for emergency response. The system would use a relay station to control the unmanned aerial vehicle (UAV), guiding it to the radiation areas and airborne radiation plumes. [25] More work on UAVs has been done in the following years by various researchers including [16], [10], and [17]. Pang's work is a more thorough plume tracking model for UAVs including autonomous mapping using Bayesian methodology. [16] Kurivnen focused his work on a multi-purpose UAV using a variety of radiation detectors, but without

autonomous control. [10] Lastly, Pollanen produced some of the first experimental data from a mini UAV over the Chernobyl area using a similar CsI detector. [17] The Bayesian methodology of Pang, the multi-purpose detection system of Kurivnen, and the experimental data of Pollanen are indicative of how this work is approached and their principles of mapping are applied to the co-robot.

The majority of robotic surveying automation has been completed using ground robots with similar intentions to the future aerial vehicle. The automation of land vehicles has been researched in the past to optimize path algorithms. To achieve this goal, it is important to first note the difference between mapping and detecting. Detection is an attempt to locate the source without regard to surveying the entire area. Models of this detection method are published by Kumar et al. [9], and Mayhew et al. [14] Kumar's robot moves at a higher speed until a large count rate is perceived, when the robot will slow down to confirm the source presence. [9] It then uses an automated scheme for sequential nuclear search based on the classical sequential testing theory. [24] Mayhew proposes a hybrid control strategy to locate a radiation source using only the intensity of the radiation. [14]

The Fukushima incident has led to several more advancements in the field of aerial radiation detection. In 2011, shortly following the incident, the Ministry of Education, Culture, Sports, Science and Technology-Japan (MEXT) began to map the affected areas. The mapping was done using a helicopter to assess the dose at 1 meter above the ground surface and the deposition of radioactive substances on the ground surface. Although these were manned helicopters and a small aircraft, it was shown that the dispersion of the radioactive releases could be seen in the surrounding areas of Fukushima from altitudes between 300-600m. [13] MEXT proceeded to take samples of the area until 2013, as seen in Figure 1. [5] This process was then optimized by Sanada et al., for an autonomous unmanned helicopter (AUH). A detection system composed of three $LaBr_3$:Ce scintillation detectors were used to replicate the MEXT data with more precision and closer proximity to the site.

As the AUH is unmanned, the vehicle could enter the 3 km barrier resulting in Figure 2.1. [20]

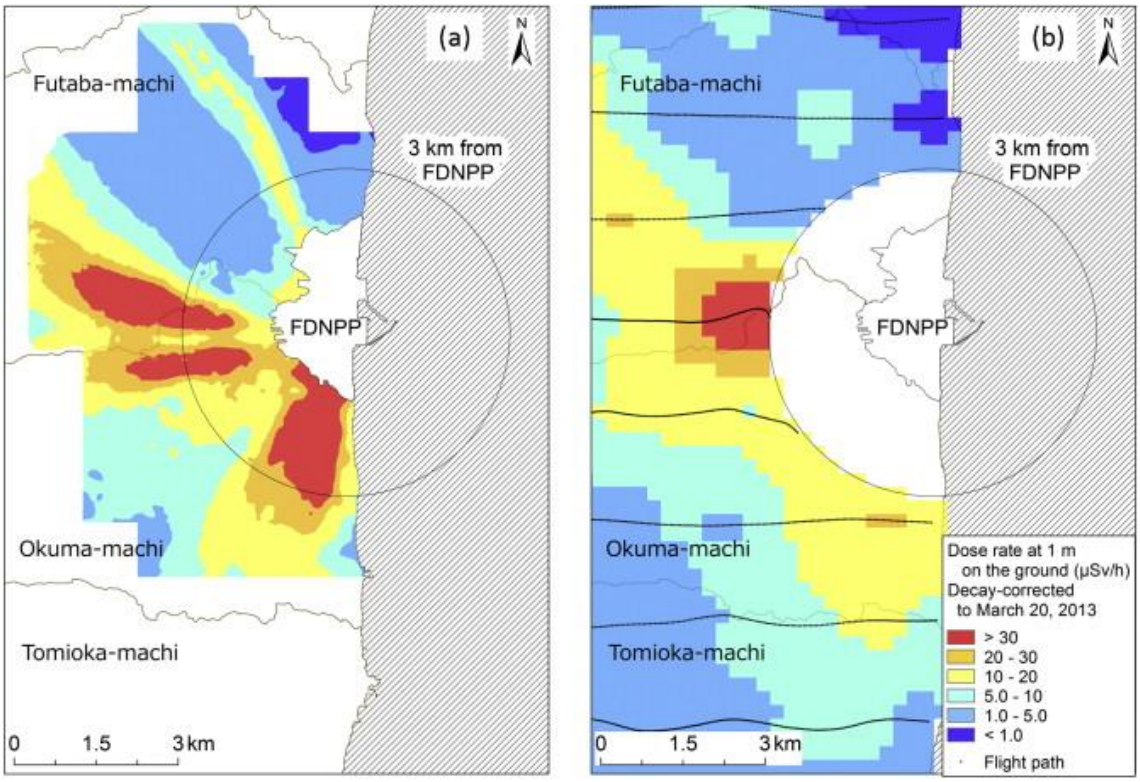

Figure 2.1: (a) Sanada et al., Measurement with Unmanned Aerial Helicopter. (b) MEXT manned Surveillance, [20]

The most relevant published work was produced by MacFarlane et al., on lightweight aerial vehicles for monitoring, assessment and mapping of radiation. The robot is a six rotor vehicle designed for both outdoor and indoor monitoring of radiation using GPS locations and a small commercial CZT detector [13]. MacFarlane uses a waypoint system in communication with a GPS signal. The research vehicle creates a path based on the outline of the known region and a set of input parameters describing the minimum source detection activity and confidence of that activity. MacFarlane et al., proved their concept in a later study by using their vehicle to map legacy uranium mines in Cornwall, England [12].

2.2 Theory

In order to construct such a complex system, it is necessary to gain an in-depth understanding of the detection and control systems. As previously discussed, the detection system is comprised of neutron and gamma detectors, as well as analytical software. These systems are mounted on a fully autonomous mobile unit using an Arduino platform in communication with a Vicon positional system.

2.2.1 Gas-Filled Neutron Tube Detector Theory

The neutron detector used in this research is a B-10 (boron) lined detector with a cylindrical aluminum shell. The boron lining is 96-100% enriched B-10, as opposed to the 20% B-10 found in nature. An aluminum shell is used due to its small neutron cross-section, resulting in a low probability of interaction with thermal neutrons. Typically, a neutron entering the tube will interact with the B-10 solid lining, producing a lithium nucleus and an alpha particle from the reaction in Equation 2.1.

$$ {}^{10}_{5}B + {}^{1}_{0}n \rightarrow \begin{cases} {}^{7}_{3}Li + {}^{4}_{2}\alpha & 2.792\ MeV\ (Ground\ State) \\ {}^{7}_{3}Li^{*} + {}^{4}_{2}\alpha & 2.310\ MeV\ (Excited\ State) \end{cases} \qquad \textbf{\textit{Equation 2.1}} $$

The resulting pair rebounds in different directions, depositing their energy in the gas while creating primary ion pairs. A single thin wire, running down the axis of the tube, acts as an anode which attracts the electron pairs creating a pulse. The resulting amplitude of the pulse is dependent on which of the two particles is sent into the gas while the other leaves the tube. The energy accumulated is described by Figure 2.2 with each particle having a given differential pulse height spectrum. The rectangular shape is idealized as a result of the equal probability of the particles being sent in any direction and depositing the resulting energy.

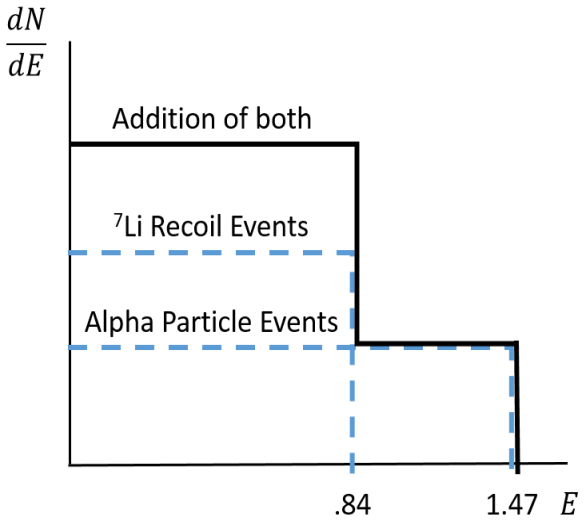

Figure 2.2: Idealized Pulse Height Spectra for B-10 Lined Proportional

Gas-filled neutron detectors may be highly compact and straightforward; however, they can only detect thermal neutrons. Neutrons do not exist naturally outside of a nucleus, and unbound neutrons have a half-life of just over 10 minutes. For a neutron to escape from the nucleus, it must overcome its binding energy, typically 7 to 9 MeV, [6] causing in high-speed neutrons. As a result, the neutron speed must be moderated using large neutron-scattering cross-section materials. Once the neutrons have been reduced to thermal speeds, the detector gas has a much higher probability of interaction with the neutron due to the high cross section of thermal neutrons.

As neutrons are rarely found to exist naturally, the observation of neutrons can be vastly important, especially for non-proliferation uses. Although it is difficult to characterize an element from just neutron energies, the addition of gamma spectroscopy helps greatly, as most neutron emitting materials also emit photons.

2.2.2 Cesium Iodide, Thallium Activated Gamma Spectroscopy Theory

The photon detector used in this research is a cesium iodide, thallium activated (CsI(Tl)) scintillation detector. This detector was chosen as it is one of the brightest scintillators known, with 54-59 photons/keV [18]. This is aided by the fact that the crystal is 1 inch square by 2 inches, which is relatively large and allows for high sensitivity to radiation. As the vehicle has only short amounts of time to measure an area, the larger quantity of data captured, the better the picture. The CsI(Tl) scintillator also has plastic-like mechanical properties making it very durable. There are no cleavage planes, which means that when impacted by outside forces, the crystal has no fault lines to form weak points and must first make its own crack before fracturing. In robotic situations where collisions are often impossible to avoid entirely, this is a useful property.

The CsI(Tl) scintillation detector works when the crystal emits light and a subsequent photomultiplier mechanism absorbs this light. Scintillating materials such as CsI(Tl) absorb the energy of the incoming particle and scintillate by emitting the absorbed energy as visible light. CsI, being a very bright scintillator, emits a green, almost yellow light, but other scintillators can vary in the colors emitted. It is possible for a material to be in a metastable excited state, so the emission of light can be delayed some time, ranging from a few nano-seconds to full minutes. CsI, however, tends to have an almost immediate release of light (from .7 to 3μs) [23] making it easier to see all events.

Inorganic scintillators emit light due to their electron band structure found in the crystal. Scintillation occurs when an electron is excited out of the valence band into the conduction band by a particle. The electron leaves an associated hole in the valence band. The impurity in the crystal, thallium in this case, creates electronic levels in the forbidden gap between the valence and conduction band. Electron-hole pairs are then captured by these impurity centers resulting in a rapid de-excitation by discharging visible light.

Table 2.1: Properties of Typical Scintillation Detectors, [6]

Material	Light Output	Wavelength of Max. Emission	Decay Constant	Density	Index of Refraction	Moisture Sensitivity
Units	**(photons/MeV)**	**(nm)**	**(nsec)**	**(gms/cc)**		
NaI(Tl)	38,000	415	230	3.67	1.85	High
BGO	9,000	480	300	7.13	2.15	None
CsI(Tl)	59,000	560	1000	4.51	1.84	Slight
$CdWO_4$	15,000	480	1100 / 14500	8.00	2.20	None
$CaF_2(Eu)$	19,000	435	940	3.19	1.44	None
Gd_2O_2S		510	3000	7.34	2.20	None
$Lu_2(SiO_4)O:Ce$	30,000	420	40	7.40	1.82	None
Plastics	~10,000	420	2-17	1.03	1.58	None

As photons are more likely to interact with denser materials, most scintillation detectors use high density materials, as can be seen in Table 2.1. The table also confirms the high intensity light output of the CsI detector. The table also notes two disadvantages, the relatively slow 1000 nanosecond decay constant and the slight moisture sensitivity. The moisture sensitivity is important as it means that higher altitudes could potentially affect the detector's performance. Although the light release is almost immediate, the relatively slower decay rate means the detector will achieve higher dead times faster. Dead time is defined as the amount of time the detector needs to reset to its baseline before it has the ability to observe the next event. A high flux of events can cause the pulse to keep increasing not allowing a quick reset and increasing the dead time significantly.

A photomultiplier is then needed to take the small quantity of light and amplify it to a measurable quantity. To reduce the size of the detector, a silicon photomultiplier (SiPM) is used in combination with the CsI crystal. A SiPM is a collection of avalanche photodiode (APD) arrays on a silicon substrate. There can be as many as 1000 APD per square millimeter, but with a large crystal, larger APDs can be used. When a voltage is placed across the SiPM, the device becomes a semi-conductor. When light is absorbed by the silicon, the energy is transferred to a valence electron, transporting it to the conduction band, creating an electron-hole pair. When sufficient voltage is applied across the SiPM, a

charge carrier created by the absorption will be accelerated enough to create secondary charge pairs. This process is repeated until an electron cascade is seen in all APDs that absorbed the light. The energy of the light can then be determined based on how many APDs detected the initial occurrence. As a current is produced by the electron cascade, the voltage is reduced below the breakdown level and the SiPM loses its semi-conductor properties, allowing for it to reset to the initial state.

Once the energies of each photon emission are calculated, they are split into 4096 bins of equal energy ranges. The 4096th bin contains all of the counts found to be greater than the upper energy limit. Once all the counts are recorded over a specified amount of time, the background counts can be subtracted and the resulting peak will characterize materials based on the equivalent energies. The biggest disadvantage to SiPM is their high level of noise, but fortunately most of the noise is usually located at the front end of the spectrum. This means with higher energies, their photon energy resolution can still be excellent.

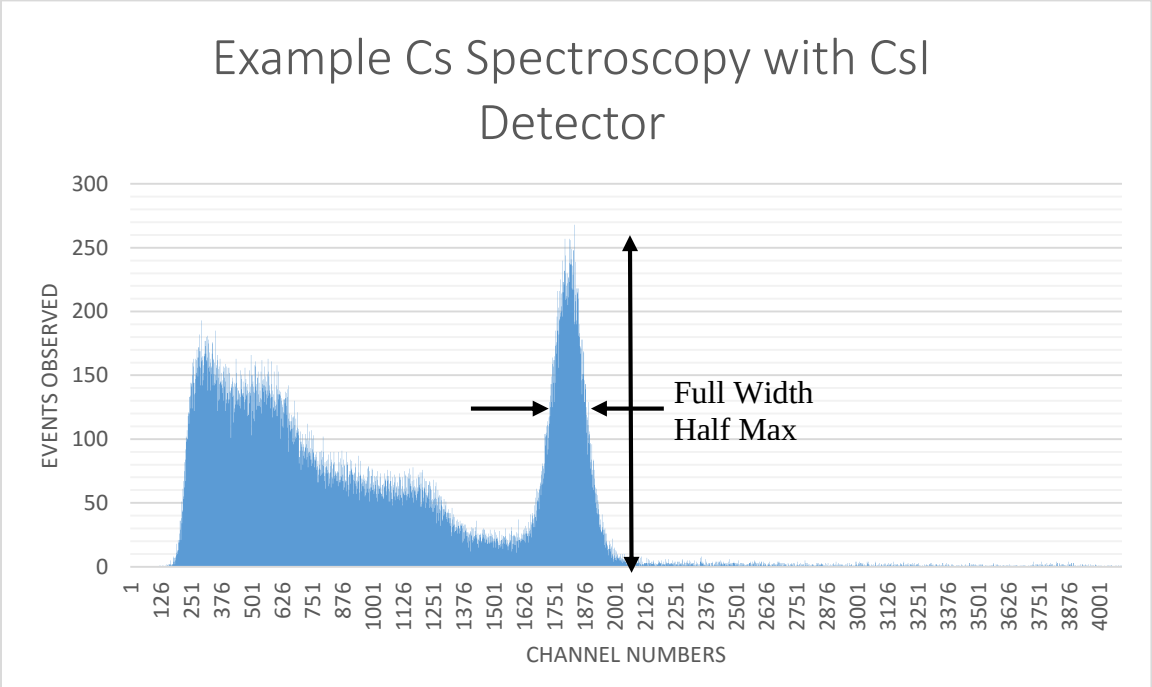

Figure 2.3: Example Cs-137 Spectroscopy with CsI Detector

Resolution of a peak can be determined by taking the full width at half of the maximum peak and comparing that to the energy at which the peak is centered. This specific detector has a given resolution of 7.2% at 662KeV. Example Figure 2.3 shows this resolution using our CsI detector with the width approximately 140 channels over the max peak channel of 1812, resulting in a 7.7% resolution at 662KeV. Although the resolution is good, the weakness of this detector is the dead time caused by the slow decay time of the photon emission. The average decay time is of around 1 μs, which is close to four times slower than NaI(Tl) and as much as 100 times slower than some other inorganic materials. As a result, in high intensity radiation fields, there is a buildup of photons that continue to hit the detector before the crystal "resets" to its initial state. This creates dead time during which the number of counts missed cannot be determined exactly. The CsI(Tl) is therefore limited to around 5,000 counts, as seen in Table 2.2. The limits are later verified via testing and the results are given in Section 4.3.

Table 2.2: CsI Detector Specifications [8]

SIGMA50 CsI Detector Specifications	
Detector Geometry	1" x 1" x 2" CsI(Tl) Detector
Energy Range	50 keV – 1.5 MeV
Maximum throughput	5,000 cps
Energy resolution	< 7.2 % FWHM @ 662 keV (21ºC operation)
Number of Channels	4096 (12 bit)
Power consumption	250 mW
Dimensions	34.5 mm x 34.5 mm x 130 mm
Weight	300 g
Operational temperature range	-10 to 40ºC

2.2.3 Vicon Positional System

The Vicon positional system is used extensively in this research as a method of determining the exact location of the vehicle. The Vicon system uses a set of reflective markers placed on the vehicle in combination with infrared cameras to determine location

based on triangulation. Calibration of the system is done by using a “wand” of known measurements and waving it in front of all 12-16 cameras. Using the distance to each of the markers on the wand, the cameras can determine their distances from each other as well as the distance from the wand. A similar trianglular device is then used to set the origin of the x and y parameters, with z facing upwards. It is important to know where the origin is as the Vicon system returns location of the objects with respect to the origin.

Each vehicle is outfitted with markers in view of as many cameras as possible. It is important that these markers are not symmetrical to avoid ambiguity in the orientation. As the Vicon system depends on the reflectivity of the markers, it is also important to cover any other sections of reflective material on the vehicle to avoid misleading the cameras. The Vicon system can then track any vehicle in the chosen area provided that a sufficient number of cameras can see the markers. The benefit of this system is the ability to consistently locate the vehicle to within one millimeter of error in a three dimensional region. This error is determined in the camera calibration and is shown in Figure 2.4.

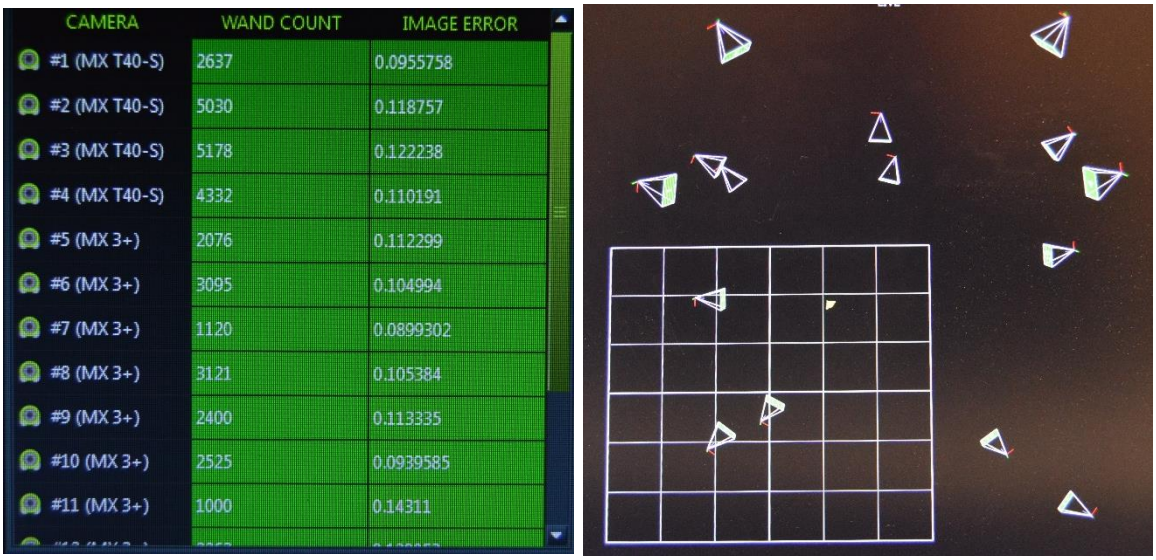

CAMERA	WAND COUNT	IMAGE ERROR
#1 (MX T40-S)	2637	0.0955758
#2 (MX T40-S)	5030	0.118757
#3 (MX T40-S)	5178	0.122238
#4 (MX T40-S)	4332	0.110191
#5 (MX 3+)	2076	0.112299
#6 (MX 3+)	3095	0.104994
#7 (MX 3+)	1120	0.0899302
#8 (MX 3+)	3121	0.105384
#9 (MX 3+)	2400	0.113335
#10 (MX 3+)	2525	0.0939585
#11 (MX 3+)	1000	0.14311

Figure 2.4: Left -- Vicon Camera Calibration Error (mm), Right -- Vicon Camera Setup

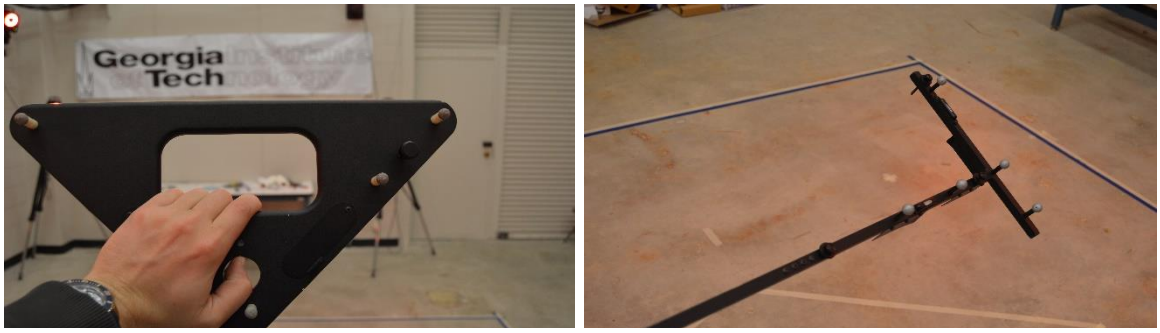

Figure 2.5: Left -- Origin Triangle to set Origin, Right – "Wand" used for Vicon Calibration

Figures 2.5 depicts the camera setup and orientations with their interface that allows for a visual image of the vehicle as seen by the cameras. The object in the middle is the vehicle as portrayed by the Vicon system. Figure 2.6 and 2.7 depict the triangle and "wand" used for calibration. On each of these devices, the gray spheres are the reflective markers detected by the cameras. The main disadvantage of the Vicon system is the limited range of the area and locations in which it can be used. However, it is appropriate for testing and calibrating the system before future work is done to implement GPS or other tracking options.

2.2.4 Arduino System and Its Shields

An Arduino system was selected as the best on-board processor for the purpose of the experiment. Arduino microprocessors come in a multitude of sizes, speeds, and powers making them very versatile. The microprocessor is coded using C++ with Arduino's proprietary code compiler. As with all C++ coding, it is important to make sure to implement all the proper libraries so that the code can work efficiently. The Arduino UNO board is used in this project due to its simplicity. The UNO, as seen in Figure 2.8, has a total of 32 pins and uses an ATmega328 as its microprocessor. The UNO is programed by sending a program through its USB port which the processor then continuously runs on loop. Alone, the UNO does not have much functionality, but the Arduino hardware systems have also been developed extensively to include many other components, such as shields, with open source libraries. Shields are accessory boards which provide additional features.

The three shields used extensively with this project are a motor shield to control the vehicle motors, a USB host shield to connect to the detector, and a XBee shield to transmit the information wirelessly back to the command station. All three shields have headers on the sides which allow the boards to communicate with other boards attached through these pins. It is important that each pin is used only once to prevent the signals from being jumbled.

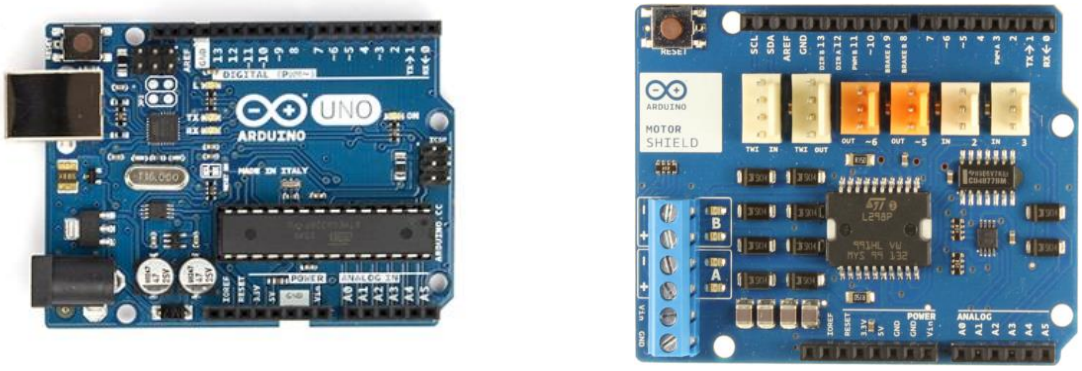

Figure 2.6: Left -- Arduino UNO Board, Right -- Arduino Motor Shield

The motor shield is used to control both motors on the vehicle as depicted in Figure 2.9. The shield uses a total of six digital pins to transmit the state of the motor. A pair of pins controls the speed of each motor, another pair controls the direction in which the motors are turning, and the last pair controls the motor brake, which stops the motor entirely. The pins to control the power to the motor use pulse width modulation (PWM) to give a range of possible speeds. The power is set on a scale of 0-255, and a full pulse is sent for a fraction of the time proportional to the amplitude's fraction of 255. For example, if a 127 is chosen, the pulse will be at full power for half the duration and at 0 for the other half, averaging out to 127.

An Arduino USB host shield in Figure 2.10 is used to interface with the USB based gamma detector. For the RC vehicle, this was not needed as an RS 232 Ethernet connection was connected directly to the XBee shield. The USB host is controlled using a library

constructed specifically for the shield. The USB detector can then communicate with the control center and relay the collected data. The USB shield uses four SPI (Serial Peripheral Interface) pins to communicate with the micro-processor. SPI is a serial data interface similar to standard serial communication such as UART used by the XBee shield, but has no need for extra start and end bits for communicating data. SPI can also be used to communicate with multiple devices on the same ports by using a slave select, but only one device is used in this project.

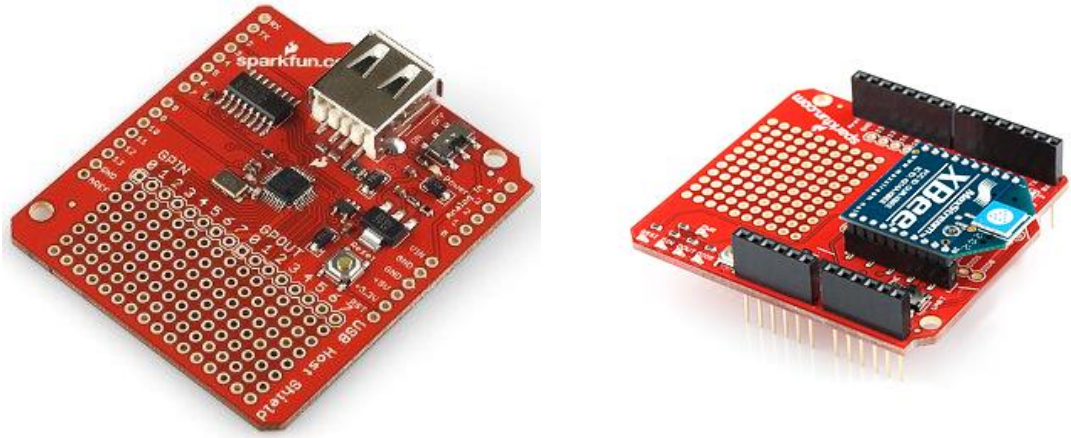

Figure 2.7: Left -- Arduino USB Host Shield, Right -- Arduino XBee Shield

The third shield is the XBee shield show in Figure 2.11, which is used to communicate with the command station wirelessly. The XBee shield hosts an XBee chip that can communicate by radio frequency to another chip connected to the command station. These chips can communicate at different baud rates based on the processing power of the microprocessor and XBee chips themselves. The baud rate refers to the quantity of bits per second that can be transferred between the two devices. A typical baud rate of 9600 would be able to transmit that many bits per second, or the corresponding number of bytes. There are also 2 modes for the XBee shield, UART and Dline. UART sends all signals that go

through the serial port to the command station. Dline sends only the information that is relayed through the Dline-specific pins. This can be useful if the processing of the data is done on the micro-processor beforehand. For the purposes of this project, the XBee Shield is used in UART mode, only necessitating 2 pins to be used for serial communication. When communicating wirelessly, however, it takes on average 10 bits to send 8 bits of information as seen in Figure 2.12 where the byte are surrounded by a start and stop bit. This can be especially difficult to manage if large amounts of data are being transmitted.

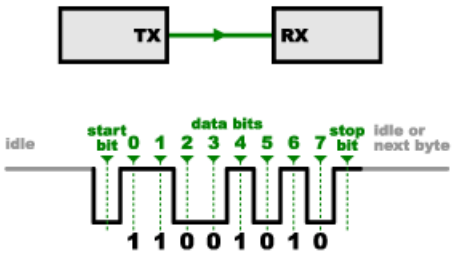

Figure 2.8: Transmitting One Byte of Information

CHAPTER 3

METHODOLOGY AND SIMULATION

3.1 Proof of Concept with RC Vehicle and Neutron Detection

The first step in completing the autonomous detection system was to demonstrate the ability to construct a small robust detection system capable of transmitting data wirelessly. A four wheeled RC vehicle was initially chosen to carry the detection system. The original co-robot was constructed in three distinct phases before the tests were run with the Vicon positional system.

3.1.1 Detector and Analysis System

The initial phase was designing a detector and analysis system that would fit all of the weight and detector limitations for the robot. In this prototype, a B-10 lined thermal neutron detector tube was chosen. The tube measures 22 cm long and weighs 166 g, making it very lightweight. Research for a light and efficient method to analyze the detector signals led to the acquisition of a Quaesta neutron pulse module (NPM). The NPM weighs approximately 200 g and is 14 cm long. When attached end to end, both the NPM and detector can easily fit into the RC vehicle. The Quaesta module was configured using a serial computer connection and QI3000 software provided by Quaesta Instruments and the Teraterm SSH. The QI3000 software can adjust the operating voltage and signal gain, display the multi-channel analyzer, and subsequently set the discriminator values. These settings are saved and loaded onto the NPM, so it can be used without a computer. For the detector, the operating voltage was set to 550V and the signal gain to 1. For the greatest efficiency, the system was configured and tested with the same PuBe sources used in the experiment.

3.1.2 Vehicle Adaptation

Next step was acquiring and adapting a vehicle for the experiments. An RC SUV car was chosen based on the high internal storage volume. The car was then disassembled to eliminate unnecessary parts, to decrease the turning radius, and to paint the surface to impede reflections. The turning motor was replaced to improve turning radius consistency. The Arduino motor shield was used to control both the speed and turning motors. For positioning purposes, the car was outfitted with infrared "markers" on the outside of the vehicle. Paired with the Vicon positional system, the car can be located to very precise positions. For controlling the car, an Arduino Uno board was used with XBee wireless component and shield. The Vicon positional system was set to a 100 Hz camera rate, allowing for commands to be sent at a maximum rate of 25 Hz to the robot. This high rate allows the cameras to correct the path of the vehicle in real-time and keep it on the predetermined path. A 9.9 V battery was used due to the power requirements of the NPM and speed motors. All components of the vehicle can be found in Figure 3.1.

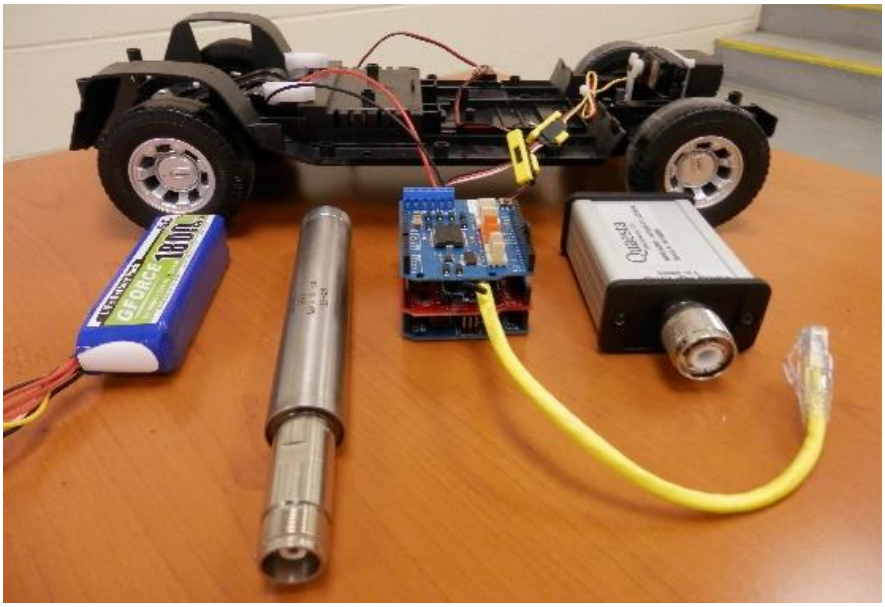

Figure 3.1: RC Vehicle Components with B-10 Neutron Detector

3.1.3 Coding and Path Planning

The last step was coding the Arduino to follow a path, correctly interface with the Vicon system, and transmit the detector data back to the control station. All of the coding was done using MATLAB software. Controls coding was integrated with the Vicon system to create the path for the vehicle, which was relayed via the XBee. After communication was established, the rest of the program ran using an open loop code, collecting information on the vehicle location without correcting the path. Two different paths were chosen with one spiraling out from the source and the other going straight away from the source at different angles. Trial and error was used to determine the exact turn radius and the area which the cameras could precisely map.

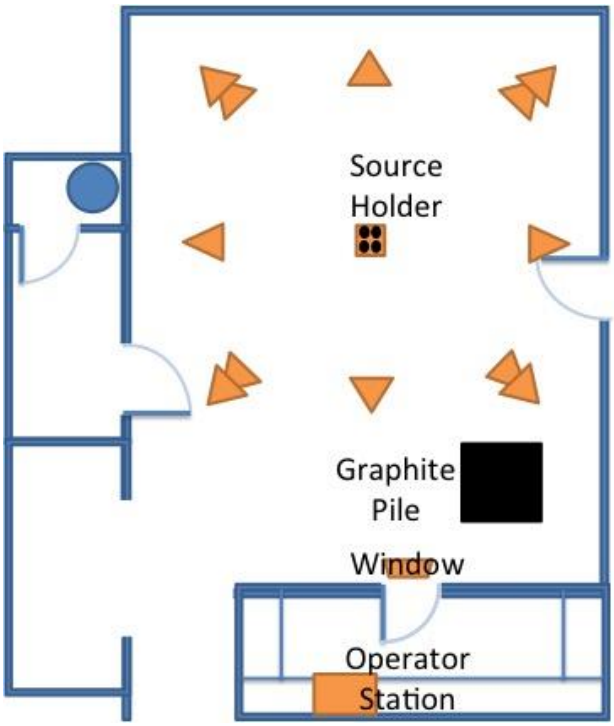

Figure 3.2: Vicon Tracker Camera Setup

The experiment was conducted in the High Bay of the Radiological Science and Engineering Laboratory (RSEL) at Georgia Institute of Technology. The room is ideal for radioactive source search experiments due to the open area, high ceilings, beam supports

for the cameras, and proper shielding. The layout of the room is shown in Figure 3.2. The source was placed in the center of the room, and the triangles mark the locations of the Vicon cameras.

3.2 Determining Detector Efficiency for Gamma Detection

To determine the maximum distance between survey locations and increase efficiency in mapping time, a detector efficiency is needed to determine what percentage of the particles that traverse the detector are absorbed. The detector efficiency was determined by detector geometry, distance from the source, and the energy of the incoming particles. The detector geometry and distance were used to find the fraction of particles that potentially interact with the detector and the attenuation of particles prior. As the detector is a minimum of 10 cm away from a source, given its position in the vehicle, the rectangular surface area of the detector is assumed as the area available for interaction. Thus Equation 3.1 is used to determine the fraction of all photons to possibly interact with the scintillator, assuming a point source.

$$(Fraction\ of\ Particles, G) = \frac{(Detector\ Width, W) * (Detector\ Height, H)}{4 * \pi * (Distance\ from\ Source, D)^2}$$

Equation 3.1

To confirm that the fraction of particles was properly calculated, an MCNP code was constructed and run at 4 different distances of 10, 20, 30, and 40 cm. Once the fractions were found to be similar, a Cs-137 check source was used to experimentally calculate the absorption efficiency at the 0.662 MeV peak. The Cs-137 energy was the only detector efficiency tested for this work and would have to be adjust for all energies in the future. The setup shown in Figure 3.3 illustrates the cesium source being used for detector saturation with a similar setup but larger source.

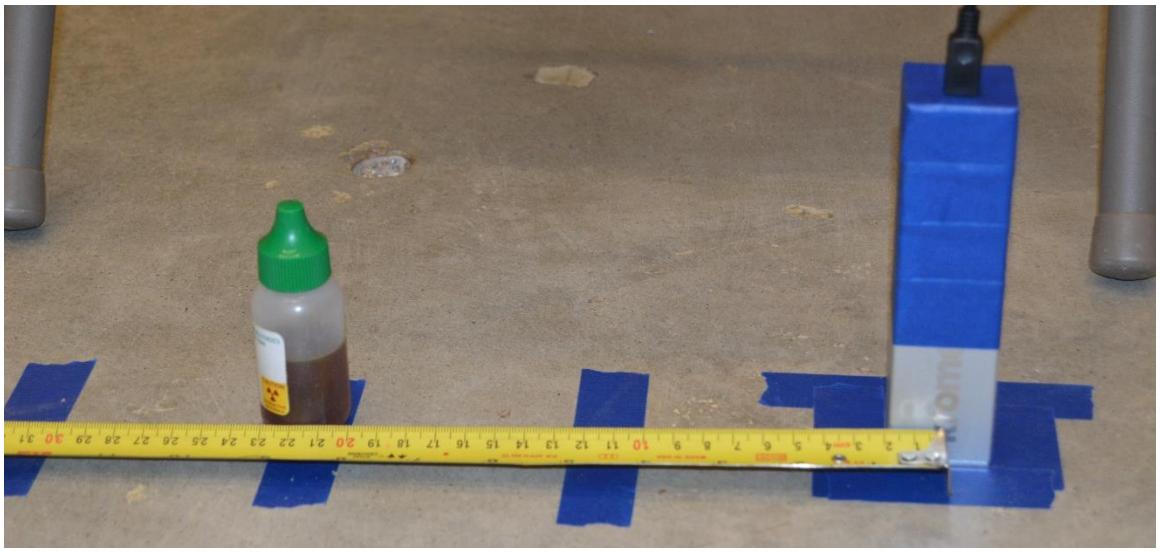

Figure 3.3: Setup for Detector Saturation Runs

The expected number of counts was determined by finding the current activity of the source using Equation 3.2 and multiplying it by the geometric fraction found above. The expected number of particles given the current activity was then needed to determine how many particles are sent in that direction.

$$(Current\ Activity, A) = (Initial\ Activity, A_o)\ e^{\frac{-t}{\lambda}} \qquad \textbf{\textit{Equation 3.2}}$$

Where t is the time passed and λ is the decay constant given by Equation 3.3 where $T_{1/2}$ is the half-life of the source element.

$$\lambda = \frac{\ln 2}{T_{1/2}} \qquad \textbf{\textit{Equation 3.3}}$$

The final factor to calculate the expected particles comes from the interaction of photons with materials prior to interacting with the scintillator. Equation 3.4 describes the

attenuation by intervening materials in which the equation length increases with each additional material.

$$I = e^{-(\mu_1 * d_1)} * e^{-(\mu_2 * d_2)} \qquad \textbf{\textit{Equation 3.4}}$$

In this case the particle is only assumed to go through air and the aluminum casing surrounding the detector. μ_1 and $\mu 2$ are the attenuation coefficients for air and aluminum for 662KeV photons, equivalent to 1.0E-4 cm^{-1} and .20 cm^{-1}, respectively. d_1 and d_2 are the distances traveled in those materials respectively, with the casing of the aluminum about .5 mm and the air distance changing based on the distance from the source. Detector efficiency is therefore equal to Equation 3.5.

$$DE = \frac{Counts\ Observed}{A * G * I} \qquad \textbf{\textit{Equation 3.5}}$$

3.3 CsI Detector Saturation

CsI scintillation detectors are known to be slower than other commonly used detector system, primarily due to their longer scintillation decay time, as mentioned above. This detector is quoted to cap out around 5,000 counts per second before the dead time becomes too large for the detector to manage.[8] As the experimental source activities can be unknown, the detector was tested with a relatively large cesium source at close proximities to see its effects. The same setup as in Figure 3.3 was used, but used a larger 262 μCi cesium source. The source was initially placed 150 cm and brought closer to the detector in increments of 10-25 cm.

The detector was also run several times while connected to the micro-processor to determine the rate at which counts could be transmitted wirelessly. This was done with the

same source, which moved periodically closer to the detector until the counts per second no longer increased.

3.4 Simulation of Terrestrial Co-Robot

The initial co-robot demonstrated the feasibility of the autonomous detection concept, but needed further development to have autonomous control for radiation mapping. The detection system was also aggrandized to include the gamma detection using a CsI detector. To goals above were attained by developing an algorithm, assembling a new vehicle, and the testing with the Vicon positional system.

3.4.1 Coding and Path Planning

The algorithm for the vehicle controls was the first step. The algorithm was a combination of mapping and detection algorithms. With simple area geometries, most of the mapping is based on Boustrophedon Cellular Decomposition [1]. At the base, the algorithm follows a simple path as shown in Figure 3.4. When obstacles are placed in the area of interest, multiple cells are created on either side of the obstacle until all cells can be reunited as seen in Figure 3.5. Within each of the cells, the robot follows a path similar to Figure 3.4. The fewer cells that the algorithm has to construct, the more efficient the mapping is with regards to both time and data acquisition. This mapping algorithm provides an informative map, from which the initial results allow more in depth investigation of the radiation anomalies. The laws of particle travel give an estimate of the sources' locations within the surveyed area. The vehicle then approaches the points of interest to determine the location and spectra of the potential source. The vehicle repeats this process for all possible source locations.

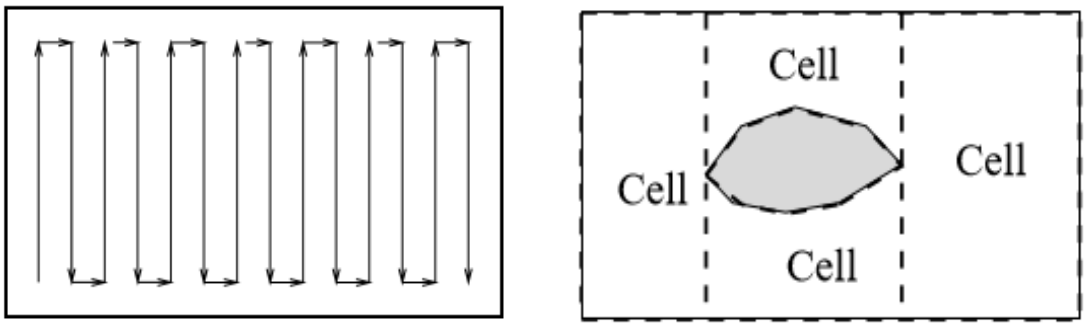

Figure 3.4: Left -- Boustrophedon Path, Right -- Boustrophedon Decomposition, [1]

For the proposed idea, the initial area would be known, and the path planning for the robot is constructed in conjunction with the level of detection confidence desired for a source of specified activity. The main advantage to this method is the ability to greatly increase the probability of finding all unique sources within the area of interest while minimizing the length of time spent on mapping. The detector takes individual counts at each location which can also give a preliminary gamma spectroscopy at evenly distributed surveying points. A more comprehensive spectrum is collected once the source location is identified and the robot moves closer to the source.

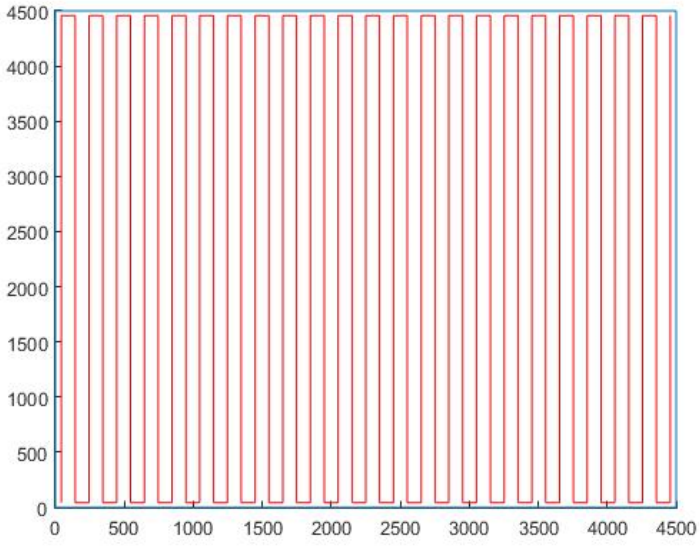

Figure 3.5: 45m by 45m Top View of Test Area 1 at 1 mCi Threshold for 1% Detector Efficiency

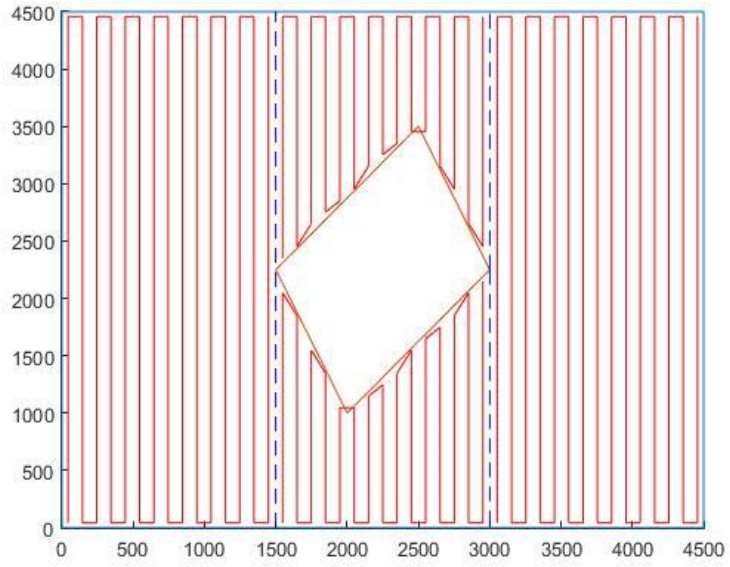

Figure 3.6: 45m by 45m Top View of Test Area 2 at 1 mCi Threshold for 1% Detector Efficiency

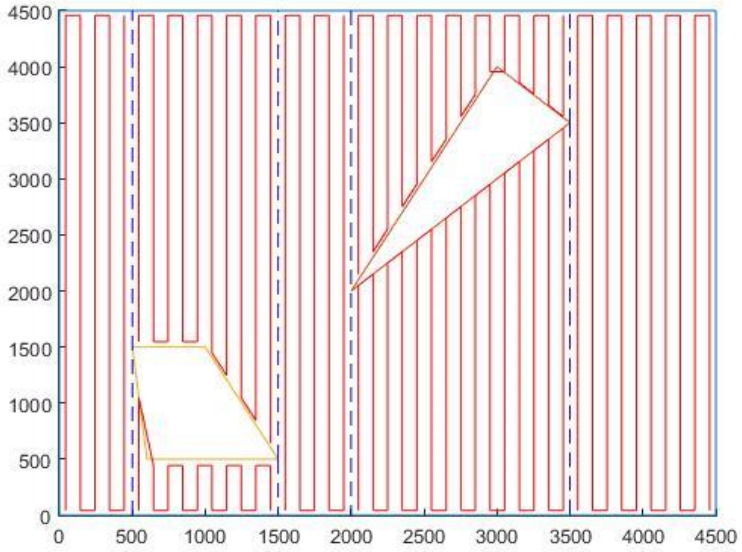

Figure 3.7: 45m by 45m Top View of Test Area 3 at 1 mCi Threshold for 1% Detector Efficiency

The algorithm is able to take a known area and map the area, as well as set a path throughout the cells. Figures 3.6, 3.7, and 3.8 illustrate the three different scenarios that are similar to those tested with their corresponding paths. All of the cells were completely traversed by the robot to ensure that all of the radiological sources are detected. Only once all the check points had been surveyed did the vehicle approach the locations of interest within the mapped area. Currently the algorithm has some limitations. The first is difficulty avoiding multiple objects aligned vertically on top of each other. The second limitation is that no two points can share an x coordinate as it currently sweeps from left to right looking for all points in the region of interest, limiting each x coordinate to one point. Lastly, the current algorithm requires the search area to be a rectangle. Solutions to these limitations are discussed thoroughly in future work.

The path length is dependent on several variables, which are taken into account for the algorithm. The survey locations are determined by using the detector efficiency calculated in Section 3.2 in combination with a threshold activity of the desired sources. The threshold activity is the level of activity the robot is trying to find with as much certainty as possible. Using the background rate plus two standard deviations for a 95% confidence threshold activity, the distance between each check point is determined by Equation 3.6.

$$SourceThreshold(Bq) = \frac{(Detector\ Width,W)*(Detector\ Height,H)}{4*\pi*(Distance\ from\ Source,D)^2} * Activity(Bq) * DetectorEff(Ratio) * (Attenuation, I) \qquad \textbf{\textit{Equation 3.6}}$$

This distance was then used to determine the number of survey locations that are needed to map out the entire area of interest. As would be expected, the distance follows an r-squared distribution in relation to the activity being sought. Figure 3.9 and Figure 3.10 show the effect of increasing the activity threshold to 10mCi and then to 50mCi. The

increased threshold results in a much shorter path of interest, which is proportional to the increase. It is also important to note that the distance calculated was from a single point, meaning that if the source is exactly the threshold value activity and located on one survey point precisely, it should still be recognized by all 4 points adjacent to that point.

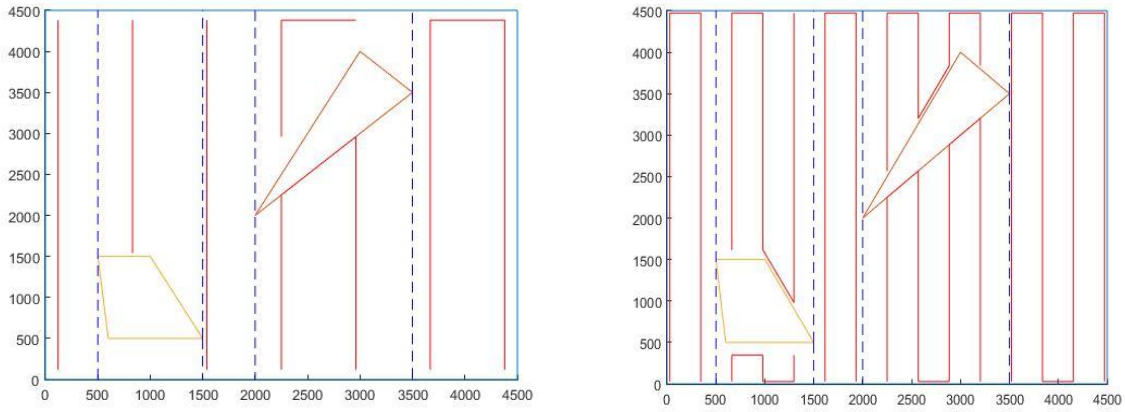

Figure 3.8: Left -- 45m by 45m Top View of Test Area 3 at 50 mCi Threshold for 1% Detector Efficiency, Right -- 45m by 45m Top View of Test Area 3 at 10 mCi Threshold for 1% Detector Efficiency

There are several limitations of the path algorithm. If a source activity is high enough to exclude certain cells from investigation, only those cells with checkpoints would be checked, but no new points would be added. This can become especially troublesome when there are only a few points present, as the resolution of the mapping is diminished, and the source could be out of the range. Another drawback is that a few of the paths determined by the algorithm intersected an obstacle, and more work is needed to avoid them completely. As the Vicon system uses the center of the vehicle to navigate from one point to the next, there was also a buffer of 10 cm added to all edges of the obstacles to give room for the vehicle to approach the obstacles.

The last part of the mapping algorithm was connecting the cells to each other. The cells were navigated sequentially beginning with the left most cell. Once the co-robot completed the first cell, it was instructed to travel to the location of the nearest checkpoint. If two

checkpoints were of equal distance from the last point, the co-robot was directed to leftmost cell. This path minimized the amount of navigation needed between cells. When traveling from cell to cell, no obstacle avoidance was implemented, but it was possible for user interaction to add a single or multiple way-points to avoid an obstacle, as seen in Figure 3.11**.** Although this is not the most efficient path with respect to time, it is still more than adequate especially for small quantities of obstacles and requires minimal processing time.

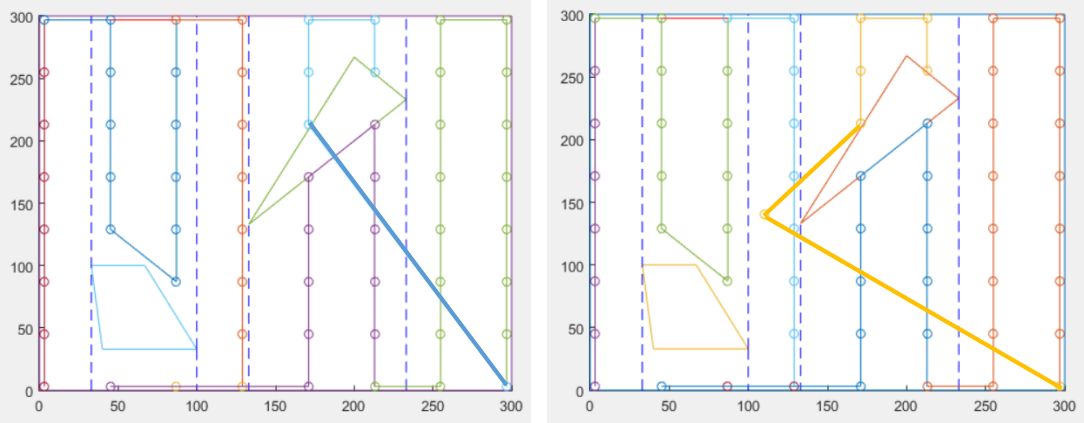

Figure 3.9: Path With and Without Way Point to Avoid Obstacle

Once the initial mapping of the area was completed, the vehicle approaches the point of maximum recorded counts. At this point, a longer spectrum was taken to characterize the source at that point. Due to the limited amount of data that could be transmitted, precise locations of high intensity sources were more difficult to pinpoint due to the plateau effect where multiple survey locations had equivalent readings.

3.4.2 Building the Track Vehicle

The second stage was the construction of the treaded vehicle. The four wheeled co-robot was determined to be inconsistent in speed and turning angle and more challenging to control precisely. For the proposed research, a treaded vehicle was used to ensure the ability to rotate in place, as a multi-rotor vehicle would be able to do. The vehicle houses

a commercial Kromek SIGMA50 [8] cesium iodide, thallium activated (CsI(Tl)) inorganic scintillator. The scintillator uses a SiPM to reduce space and weight along with very compact components. As seen in Figure 3.12**,** the CsI detector was mounted to the vehicle vertically to give nearly equal solid angles from all locations, reducing the significance of the vehicle's orientation. The height of the detector is of lesser importance for the land version which operates in a two dimensional plane, but it will need to be considered for aerial vehicle applications.

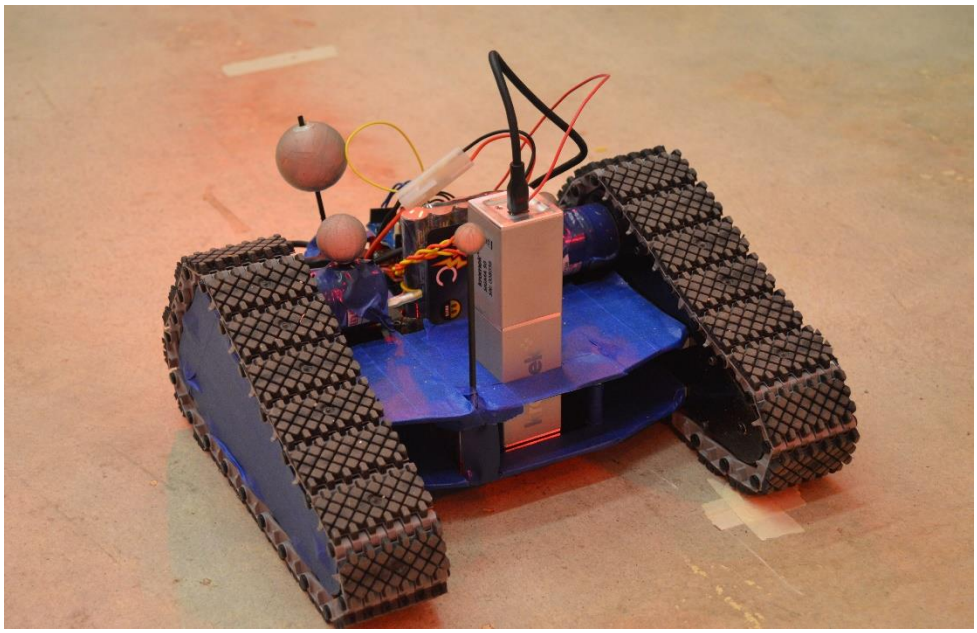

Figure 3.10: Final Vehicle Construction with CsI Detector

Communication with the control system was achieved wirelessly through a microprocessor and XBee shield, in a similar fashion to the original vehicle. The wireless channel also relayed the controls from the computer to the vehicle. All of these controls were once again coded using MATLAB to connect the VICON tracking system to the vehicle. The communication chart can be seen in Figure 3.13 below. As opposed to the first vehicle, two speed motors and no turning motors are used in conjunction with the

motor shield. The vehicle subsequently turns by controlling the speed to both treads on either side of its chassis. Both motors turning at the same speed in opposite directions results in the vehicle turning on itself, allowing for much easier navigation. The other significant difference is the use of the Arduino USB host shield to communicate with the CsI detector. The shield communicates all of the information via SPI pins to the Arduino and subsequently by serial communication to the XBee to relay the data to the command station. As the detector is a USB device, 5 V is required to power the detector and therefore a 9.6 V battery was used in order to use the motors, micro-processor and detector simultaneously. The silver markers on the final vehicle build are used by the Vicon positional system to identify the vehicle location.

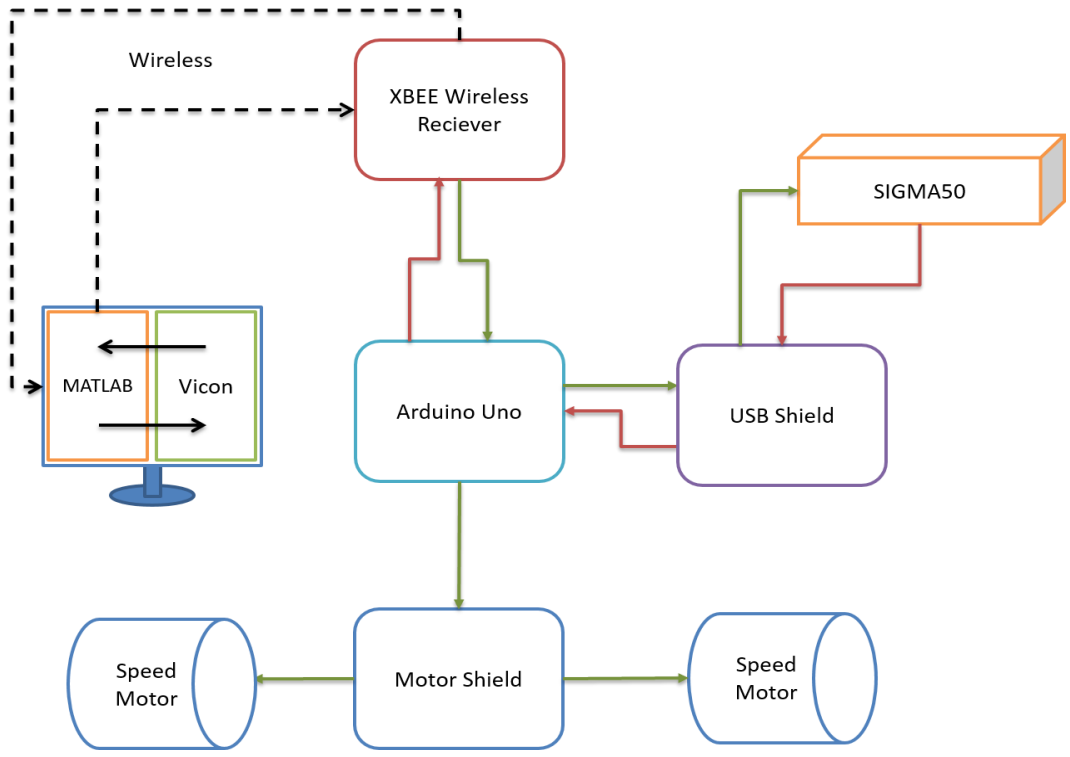

Figure 3.11: Vehicle Communication Schematic

3.4.3 Testing the Vehicle

The third phase was testing the vehicle in a controlled indoor setting using sources of known activity. All of the experiments were conducted in the Indoor Flight Facility at Georgia Tech using the Vicon positional system. Due to the restrictions of the Vicon system, the experimental area was limited to a 3 meter square space. Before the experiments began, the Vicon system was calibrated with the "wand" and origin triangle. Due to the size of the area, the two main sources used were two Cs-137 sources of 1 μCi and 262 μCi, which can be seen at varying degrees of certainty throughout the area of interest.

To test the co-robot, the source threshold for the algorithm were chosen as 100 μCi, 16 μCi, and 4 μCi. These thresholds were chosen based on the two sources and the time required to explore the whole area. Although the lowest threshold of 4 μCi is still greater than the 1 μCi Cs-137 source, the source should still be easily recognized by at least one survey location. Due to the r-squared relationship of activity to distance, multiplying the threshold activity by 4 would mean the path is halved. Since at least two survey locations would observe the source if the threshold was equivalent to the source activity, at least one should still identify the source at a 4 μCi threshold and a minimum of 50 percent chance to pick it up on the 16 μCi threshold. The time of counts was set to 15 seconds to obtain a general sense of the radiation levels before approaching the location of the maximum counts observed. First, the background counts were taken with these settings. The background counts for the 4 μCi runs were limited to 5 second count times, as the run involved over 200 different survey locations.

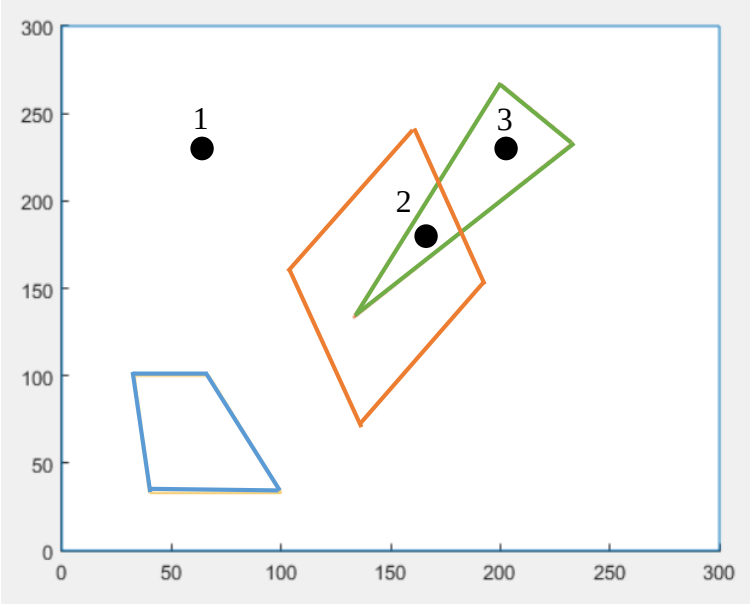

Figure 3.12: Source Locations in Area of Interest in Relation to Obstacles

The co-robot was then run for all three room configurations with both cesium sources. A combination of three source locations was used for almost all the runs, as seen in Figure 3.14, with the first outside all obstacles in the upper left hand corner. The second location is within an obstacle for both obstacle rooms. The last location is only in the two-obstacle room. For the open room, the sources were rotated throughout all three locations for both source activities. The one-obstacle and two-obstacle room had the sources placed in the second and third places, respectively, as well as the first location for both. This allows the comparison of distance to the sources and how it affects the findability given the threshold of the run.

The room setup without any obstacles was then run with shorter count times to determine at what speed the co-robot can be run with sufficient accuracy. The count times were reduced to 5 and then 2 seconds per survey location. The count time was then set at 10 seconds for several additional runs using the open room but with multiple sources present. To demonstrate the characterization ability of the detector, two Co-60 and one Na-22 check source of 1 μCi each were used in subsequent runs. The sources were placed at various distances from the smaller and larger Cs-137 sources to try to distinguish them.

The final runs were completed in an attempt to replicate the possibility of shielding around the source in the one-obstacle room. For these runs, only the larger cesium source was used. The source was shielded on 2, 3, and 4 sides with lead and concrete in order to observe the resulting gamma fluxes across the room. The last run also included the Sodium and both 1 μCi Co-60 sources to integrate aspects of shielding, shorter run times, multiple sources, and obstacles.

CHAPTER 4

RESULTS AND DISCUSSION

4.1 RC Vehicle Co-Robot Results

The robot was programmed to follow a background count path and source count path. For the first set of runs, the background path was run four times and the source path was run three times. The positions of the vehicle were recorded from the Vicon system as seen in Figures 4.1.c and 4.1.d. The counts recorded for those positions are presented in Figures 4.1.a and 4.1.b. The gradient bar to the right of Figures 4.1.e and 4.1.f represent the heat map color distribution corresponding to the measured radiation levels in counts per second, and will be used in all of the following figures.

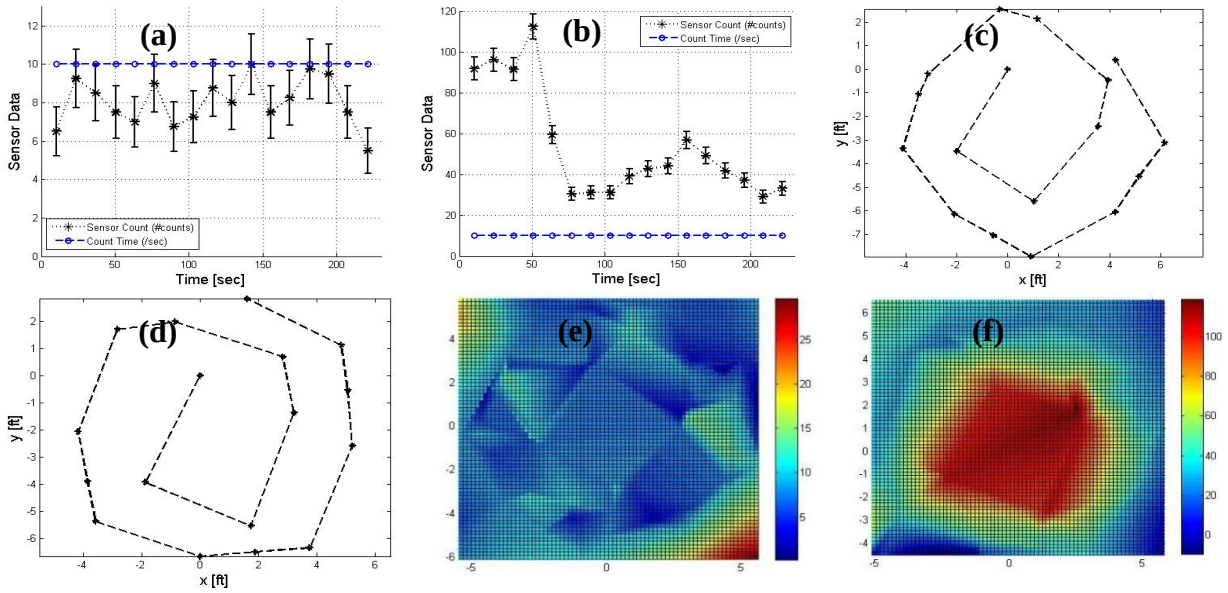

Figure 4.1: Paths of Background (a) and Source (b) Runs, Counts of the Background (c) and Source (d) Runs, Surface Plots of the Background (e) and Source (f) Runs.

In the first set of runs, a noticeable increase in overall counts above background is observed for a very large area. This is due to the constraints of the vehicle due to the turning radius. There is a difference of over 100 counts from the same background plots. This may be caused in partially because the paths were not consistently identical due to a fluctuating battery life and an open loop code algorithm, meaning that the car did not self-correct its path. From Figure 4.1.b we also notice a second peak of counts at around 150 seconds. This peak is a result of the vehicle drifting slightly off course towards the source as can be seen by the outside path of Figure 4.1.c. Another possible cause for the increase around these points is the orientation of the detector. Due to the constraints of the RC vehicle, it was not possible to add moderating material around the detector, and instead it was placed around the source. This means that the greater the surface area facing the source, the greater the chances are of the observing the neutron particle. At these points the detector is almost perfectly perpendicular to the source, maximizing the surface area exposed. Error calculations must take into account the solid angles between the cylindrical tube detector and the source. When a source is unknown in future tests, the angle will be difficult to determine, so a vertical cylindrical detector for land or a spherical detector for above ground tests would be ideal to minimize these effects.

To confirm the source, a second path was loaded on the robot in a star pattern as seen in Figure 4.2. For these runs the count times were 15 seconds each. The pauses between sets of runs were to allow time for moving the vehicle to avoid inconsistent turns. The background count rate was approximately the same. The proximity to the source gave the source runs a much higher count rate, as seen in Figure 4.2 and 4.3.

The new detector path gave a much sharper resolution image, but required human interaction to reduce both the orientation and proximity limitations. The vehicle was initially placed in close proximity to the source, about one foot away, as seen in Figure 4.2. The results gave an exceptionally high resolution of the source location and intensity.

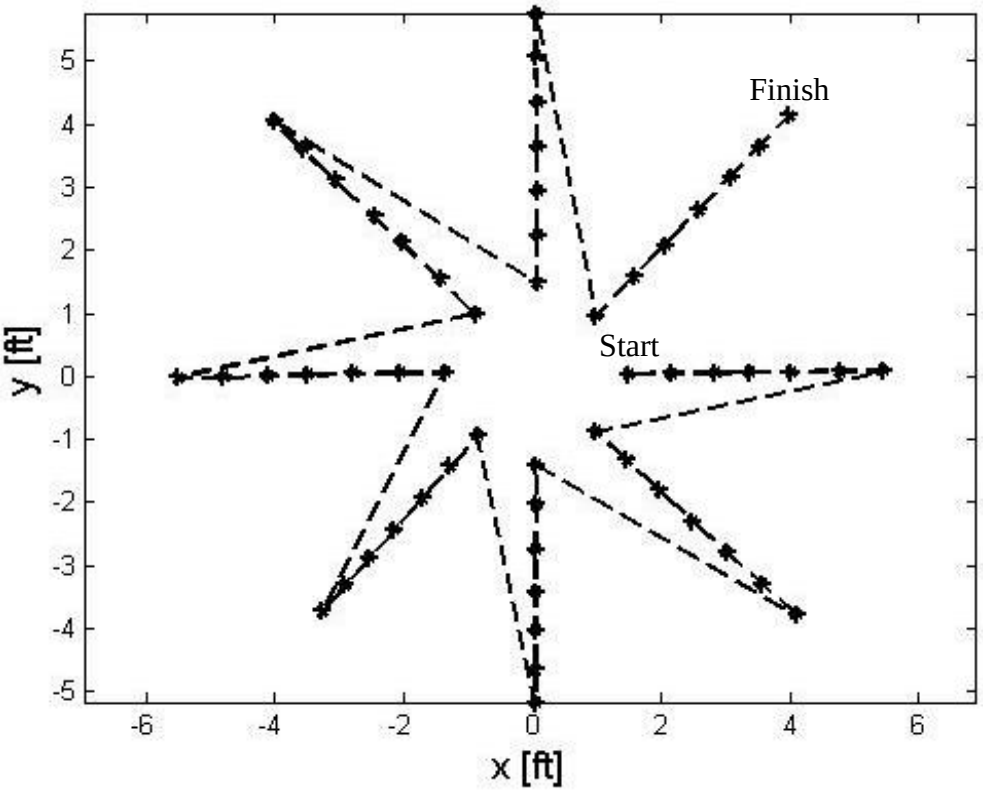

Figure 4.2: Star Path of Confirmation Source Run

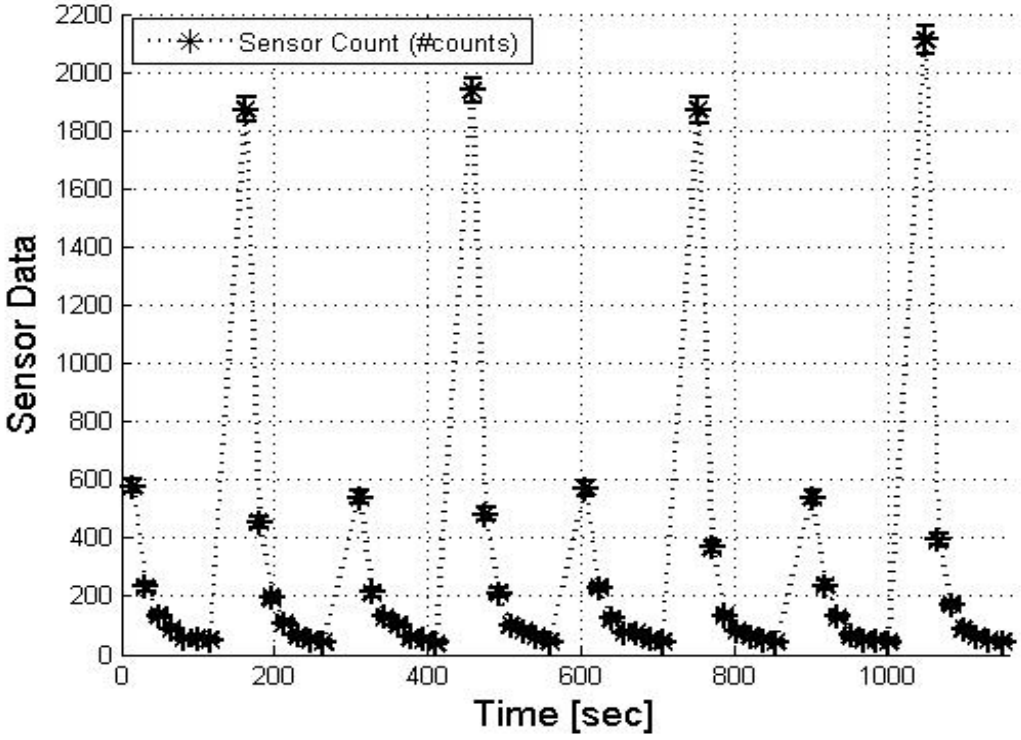

Figure 4.3: Thermal Neutron Counts from Star Path

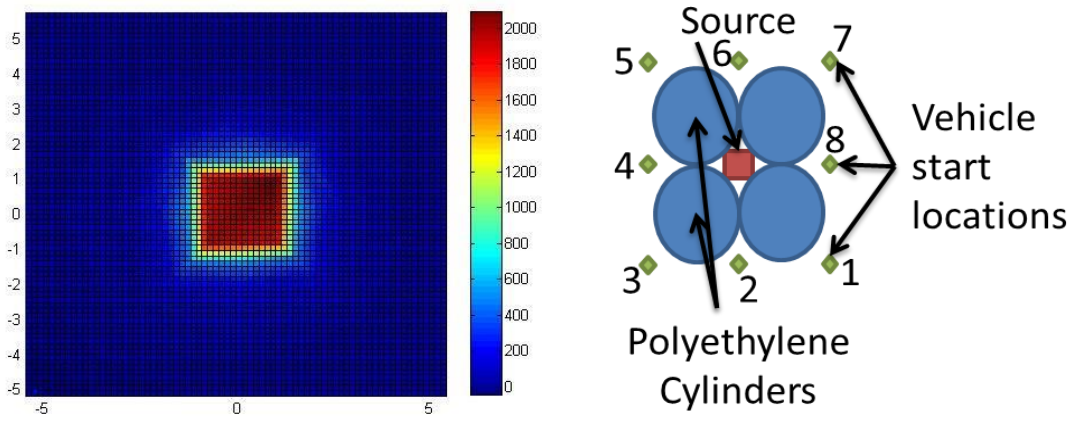

Figure 4.4: Left -- Surface Plot of Counts from Star Path, Right -- Source Moderation and Star Path Start Points

The counts reduced at a fractional rate of distance from the source, as seen in Figure 4.3 and Figure 4.4. The detector was maintained at a consistent angle, moving in straight lines away from the source allowing for all the points to be more comparable to each other. As for the increased starting level of the four points, it was observed that half the points had excessive moderation. To moderate the source down and increase visibility of the neutron, four cylinders were used as seen in Figure 4.5. As a result, half of the points had more moderating material. In future experiments it would be ideal to moderate the sources in a cylindrical method. Once the detector is thermalized, as opposed to the source, counting inaccuracies will be reduced.

4.2 Detector Efficiency Results

Table 4.1: Verifying the Surface Area Assumption for the Geometric Fraction

Distance	Geometric Fraction (G)	MCNP Results	Percent Error
10 cm	0.010268	0.009473	0.077435
20cm	0.002567	0.002479	0.034328
30cm	0.001140	0.001141	0.000488
40cm	0.000641	0.000650	0.012989

The surface area assumptions for acquiring the geometric area required verification via the Monte Carlo N Particle (MCNP) program. Table 4.1 compares the results of the MCNP code for flux of a point source through the detector compared to the fractional method described previously. The biggest discrepancy is the shortest path, but the error is still relatively small and the probability of the source being 10 cm or less away is essentially negligible. It was therefore presumed that the assumption of using the rectangular surface area was valid.

Table 4.2: Calculating the Detector Efficiency for the CsI Detector using a 1 µCi Source

Distance	Observed Events w/o Background	Current Activity, A (Bq)	Geometric Fraction, G	Attenuation Fraction, I	Detector Efficiency
10 cm	10306	30787.85	0.010268	0.989060	0.549350
20 cm	2851	30787.85	0.002567	0.988071	0.608485
30 cm	1479	30787.85	0.001140	0.987084	0.710948
40 cm	756	30787.85	0.000641	0.986097	0.646701

The results from the detector efficiency runs, using distances of 10, 20, 30, and 40 cm from the source to the scintillator, are summarized in Table 4.2. The table shows a consistent efficiency of approximately 60 percent, which is confirmed by Figure 4.6, as researched by Saint-Gobain.[19] For the purpose of these experiments the 60 percent efficiency was used, as most sources tested were cesium sources with 662KeV energy peaks. In a situation where sources are completely unknown, it would be recommended to use a smaller efficiency to guarantee the source threshold is accurate. The detector geometry would also have to be considered more thoroughly once an aerial vehicle is

chosen, as the three dimensional mapping would change the solid angles from the point source.

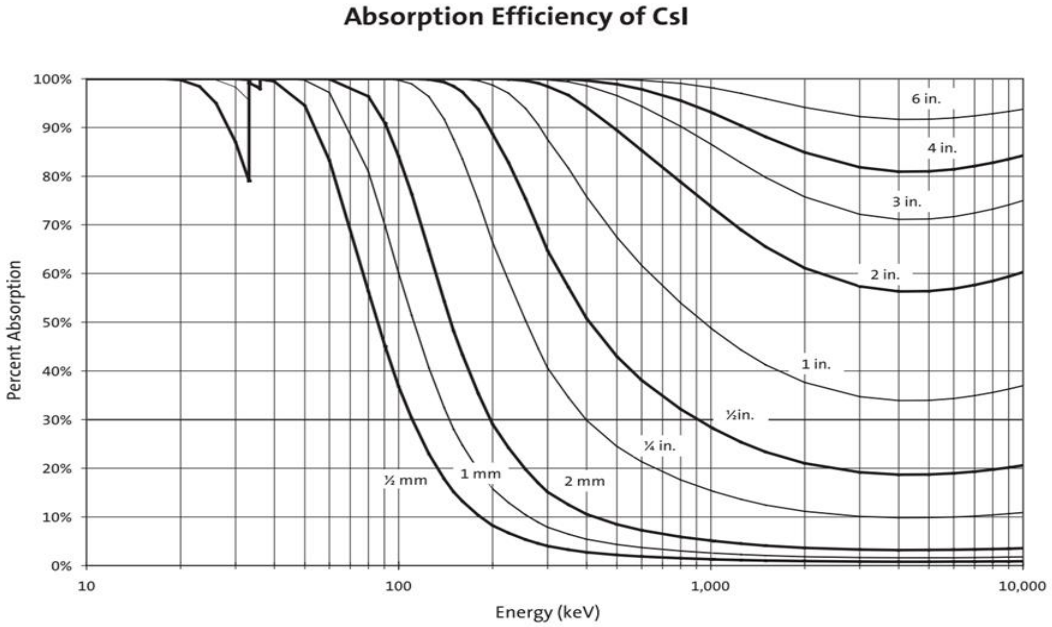

Figure 4.5: Absorption Efficiency of CsI by Saint-Gobain [19]

4.3 Detector Saturation Results

Table 4.3: Detector Saturation versus Distance from Source

Distance	Counts/sec	Minus Background	Dead Times
10	10256.283	10043.01	60%
20	6812.2	6598.925	40%
30	4003.8833	3790.608	23%
40	2570.075	2356.8	15%
50	1775.2833	1562.008	10%
60	1297.4167	1084.142	8%
70	1008.7583	795.4833	6%
80	821.08333	607.8083	5%
90	680.425	467.15	<5%
100	589.25833	375.9833	<5%
125	449.70833	236.4333	<5%
150	381.71667	168.4417	<5%

The 262 µCi cesium source was tested at 12 locations, with the distance between the source and the detector ranging from 10 cm to 150 cm. Table 4.3 outlines the distances and subsequent counts for the source. The dead time increases greatly starting 50 cm away from the detector, and as a result the count totals continue to increase, but not exponentially as would be expected as shown by Figure 4.7.

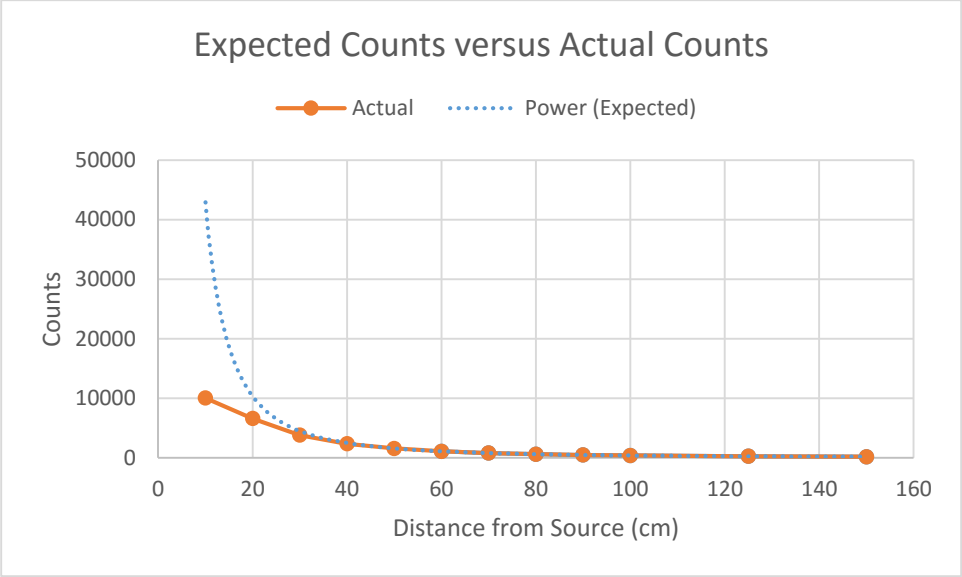

Figure 4.6: Saturation of Detector with Respect to Distance from Source

Another interesting effect of the close proximity is the shifting peak energy of the cesium source. This is quite unusual, and is likely a result of the pulse heights being only partially counted due to the high flux of photons entering the scintillator. The disadvantage to this is that even with a thorough calibration, it is difficult to characterize a high activity source when the detector is positioned closely. The detector would have to retreat from the source to take a new spectrum. This same flaw, however, is used as a precision aide for locating the source in some cases, as a different range of energy bins can be searched to pinpoint a close source. Figures 4.8 and 4.9 show a normal cesium spectrum at 60 cm, and a shifted spectrum at 20 cm.

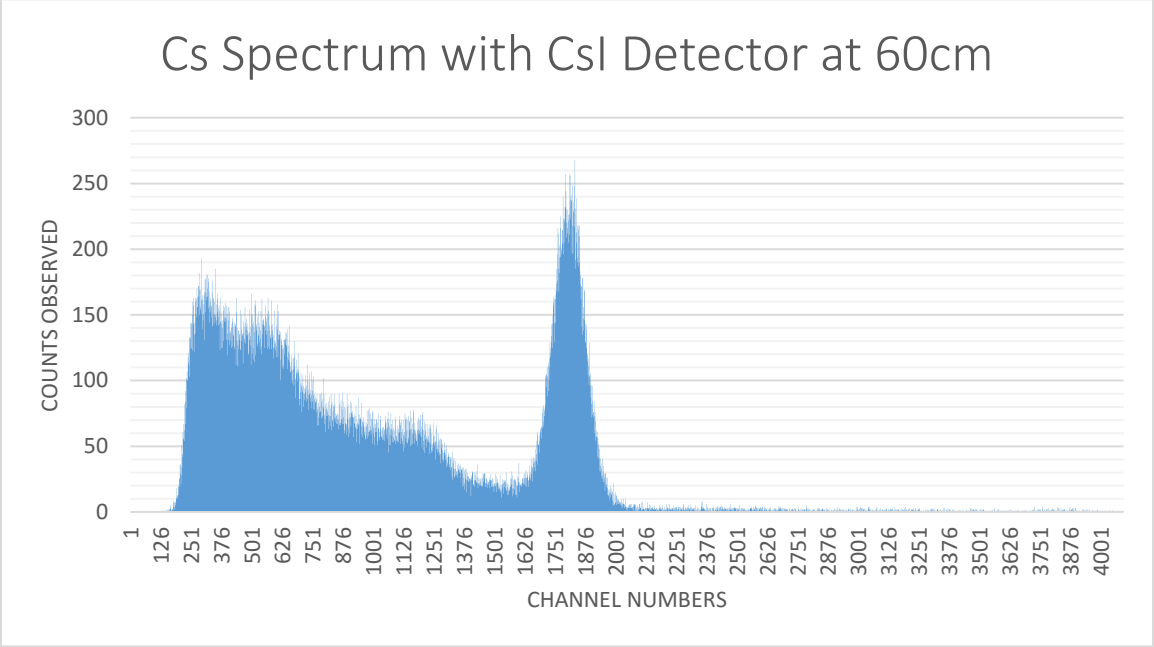

Figure 4.7: Cs-137 Spectrum with Normal Peak

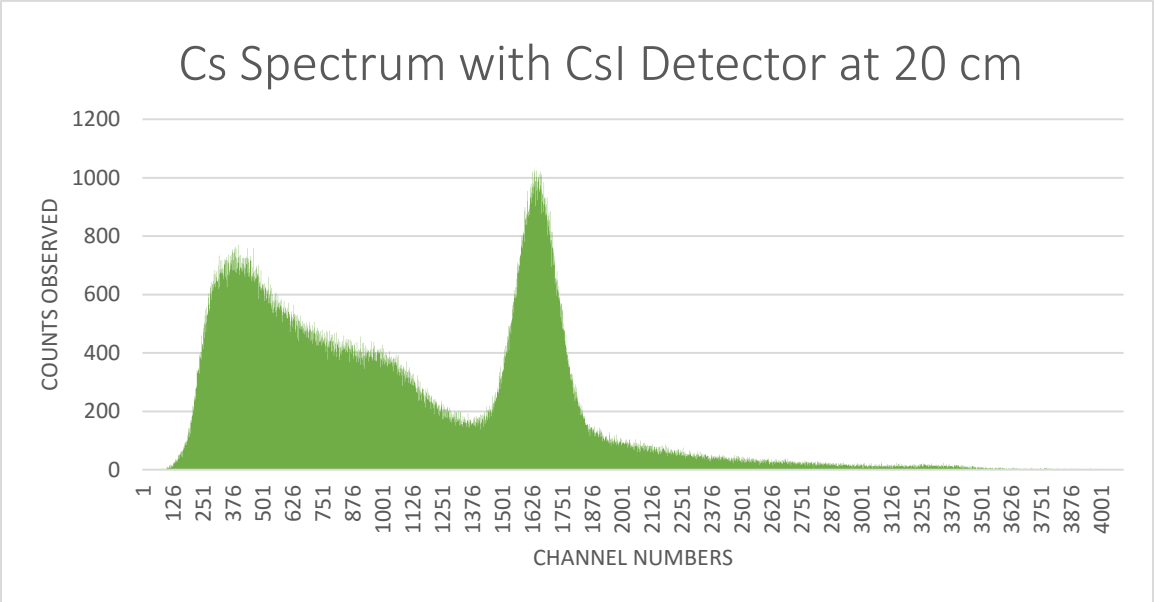

Figure 4.8: Cs-137 Spectrum with Shifted Peak

There is also another form of detector saturation in the form of the micro-processor bit processing limitations. The Arduino Uno used for this project was limited to a 38400 baud rate and could only process a maximum of 383 counts per second. This becomes problematic when dealing with higher activity sources because they can rapidly exceed this limit, causing a plateau effect to be seen throughout the area immediately surrounding the source.

4.4 Terrestrial Co-Robot Results

The three threshold activities chosen were 100 µCi, 16 µCi, and 4 µCi. The background map of the three thresholds are shown in Figure 4.10, Figure 4.12, and Figure 4.14. The backgrounds are expectedly random and do not have a large range of counts. The paths used for all three of these runs are located beside the thresholds, in Figures 4.11, 4.13, and 4.15. The square boxes and dashed lines represent the route the co-robot took, with each red circle marking a location at which a measurement was taken.

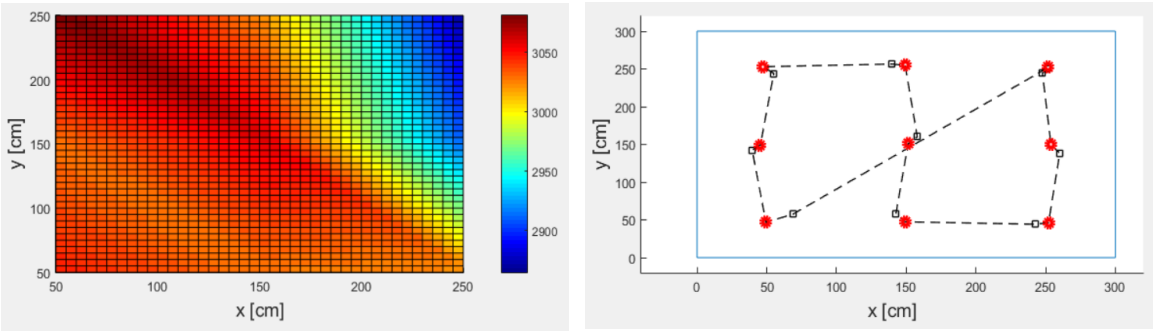

Figure 4.9: Left -- Open Room Background Surface Plot for 100 µCi Threshold, Right -- Open Room Background Path for 100 µCi Threshold

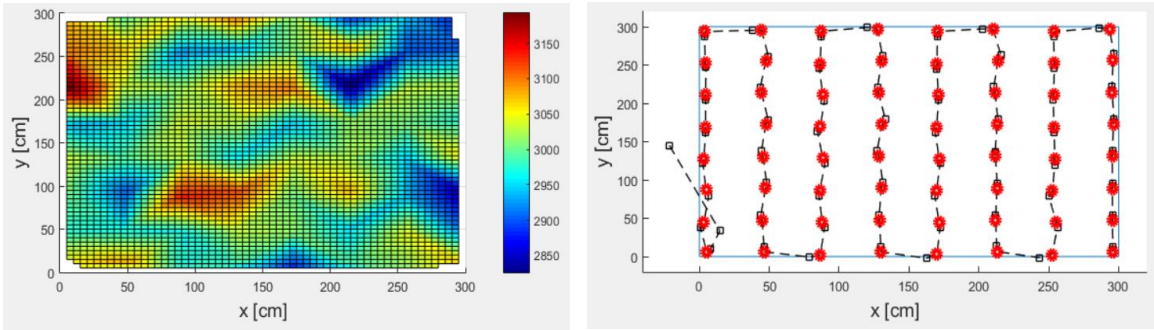

Figure 4.10: Left -- Open Room Background Surface Plot for 16 µCi Threshold, Right -- Open Room Background Path for 16 µCi Threshold

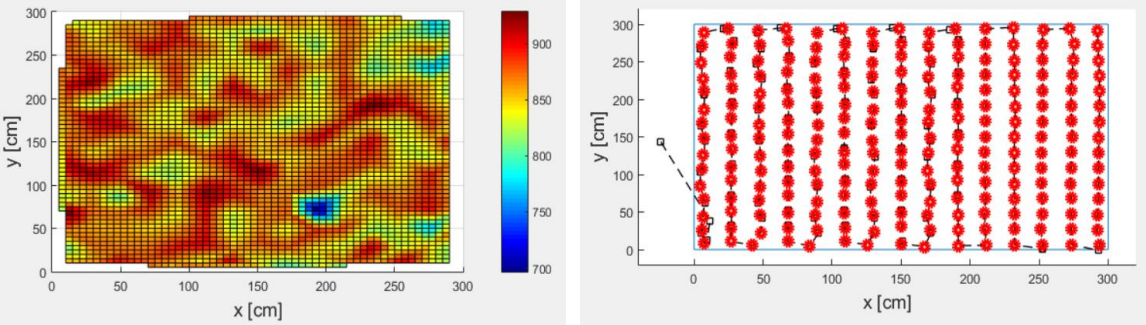

Figure 4.11: Left -- Open Room Background Surface Plot for 4 µCi Threshold, Right -- Open Room Background Path for 4 µCi Threshold

Each background survey location has a gamma spectrum which are similar to Figure 4.16. This spectrum shows a 2 minute count of the background in the center of the room and is shaped as expected, with high counts at lower energies and negligible counts at higher energies.

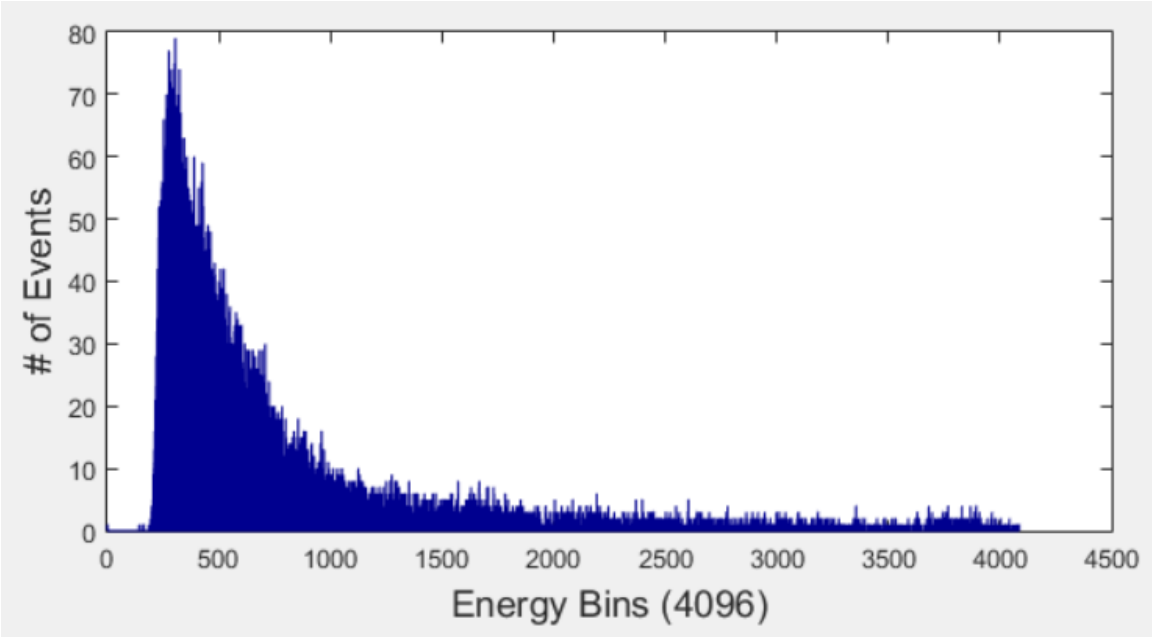

Figure 4.12: Background Spectroscopy with CsI Detector in Indoor Flight Facility

The equivalent runs in the open room were then completed for both the large and small cesium sources at location 2 for all three thresholds. Figure 4.17 shows the small Cs-137 source at the 100 µCi level, although there is a definite increase in counts in the center of

the region, the robot fails to locate the source. This is likely due to the counts needing to be higher than two standard deviations above background before being considered a point of interest. However, the robot can locate the source for both 16 µCi and 4 µCi, shown in Figure 4.18 and Figure 4.19 respectively. The 4 µCi mapping is the most precise, as would be expected, but the run time was close to twice as long despite the reduction in count time at each point. All of the paths followed for these runs were identical to the background open room paths.

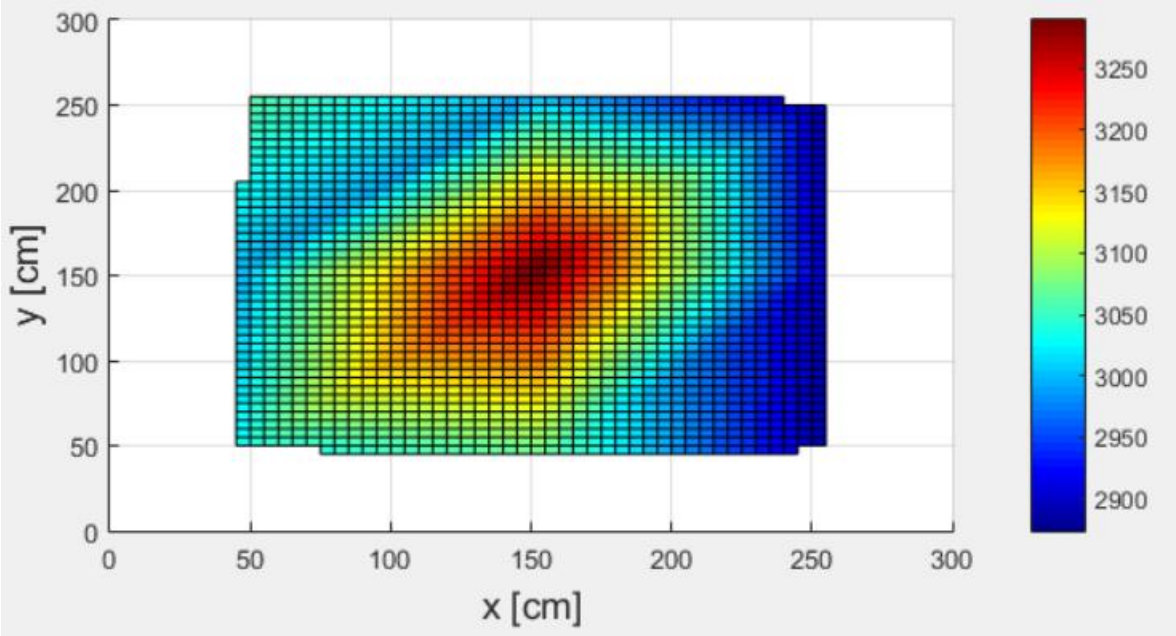

Figure 4.13: Open Room with 1 µCi Cs-137 Source Surface Plot for 100 µCi Threshold

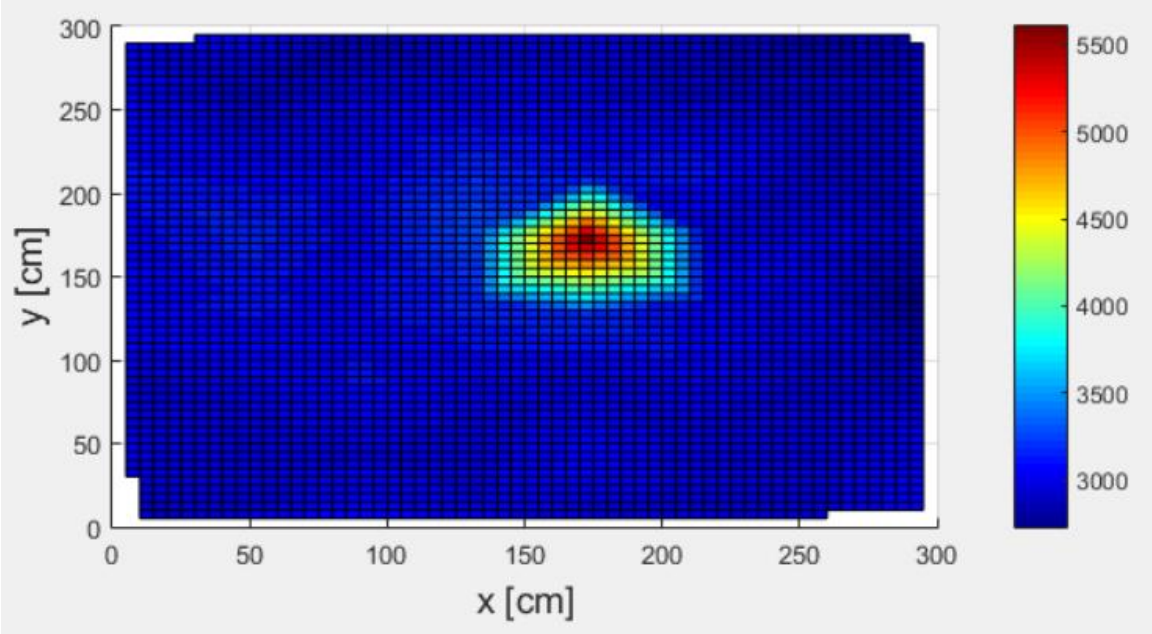

Figure 4.14: Open Room with 1 µCi Cs-137 Source Surface Plot for 16 µCi Threshold

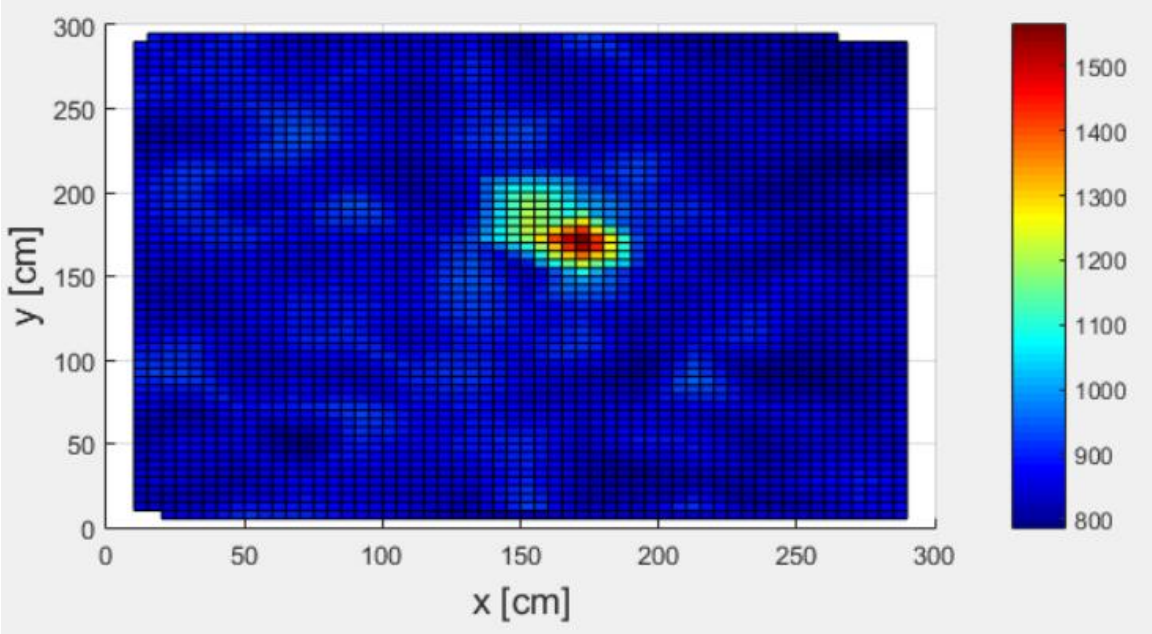

Figure 4.15: Open Room with 1 µCi Cs-137 Source Surface Plot for 4 µCi Threshold

After approaching the point of interest, the co-robot gathered the cesium spectrum in Figure 4.20 for the 2 minute counts. The peak, although small, is clearly visible and at the expected bin numbers.

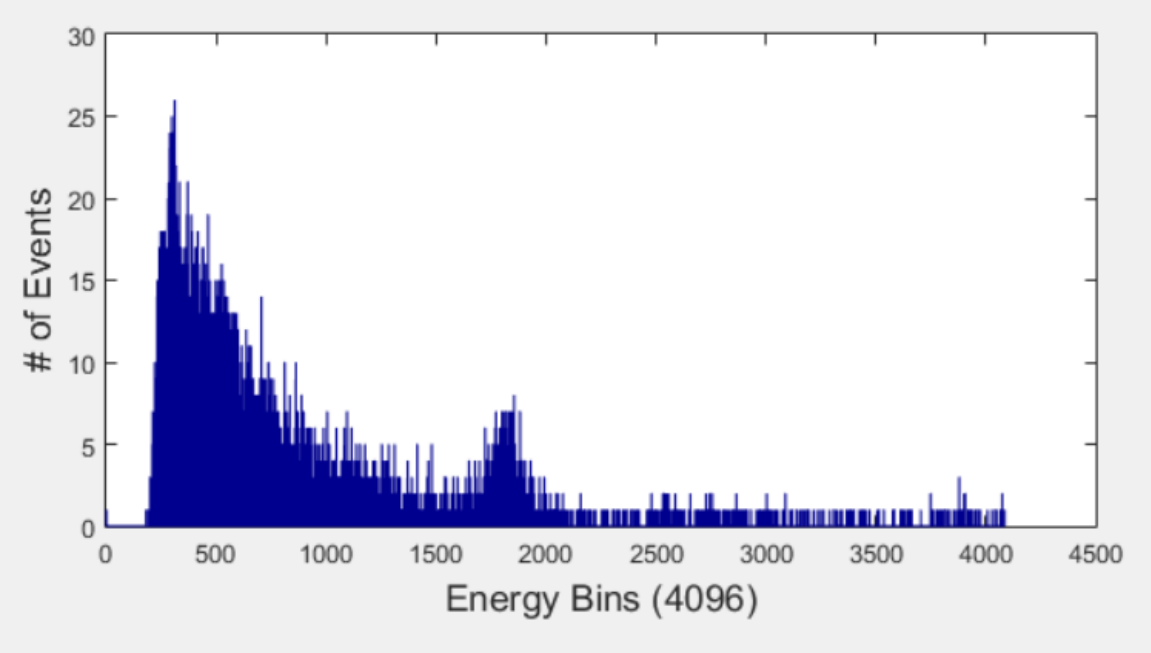

Figure 4.16: Two Minute Cs-137 Spectrum Once the Co-robot Found the 1 µCi Source

For the large Cs source, the plateau caused by the maximum count rate is easily distinguishable in Figures 4.21, and Figure 4.22. This maximum count rate is due inability of the micro-processor to transmit over 400 counts per second.

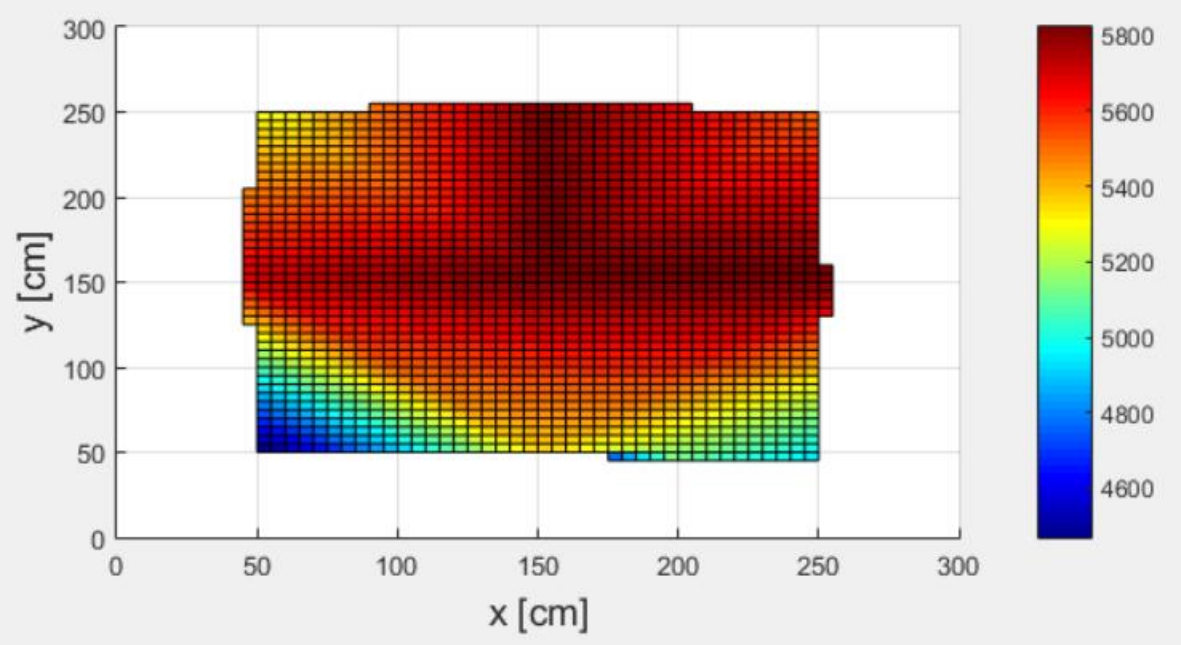

Figure 4.17: Open Room with 262 µCi Cs-137 Source Surface Plot for 100 µCi Threshold

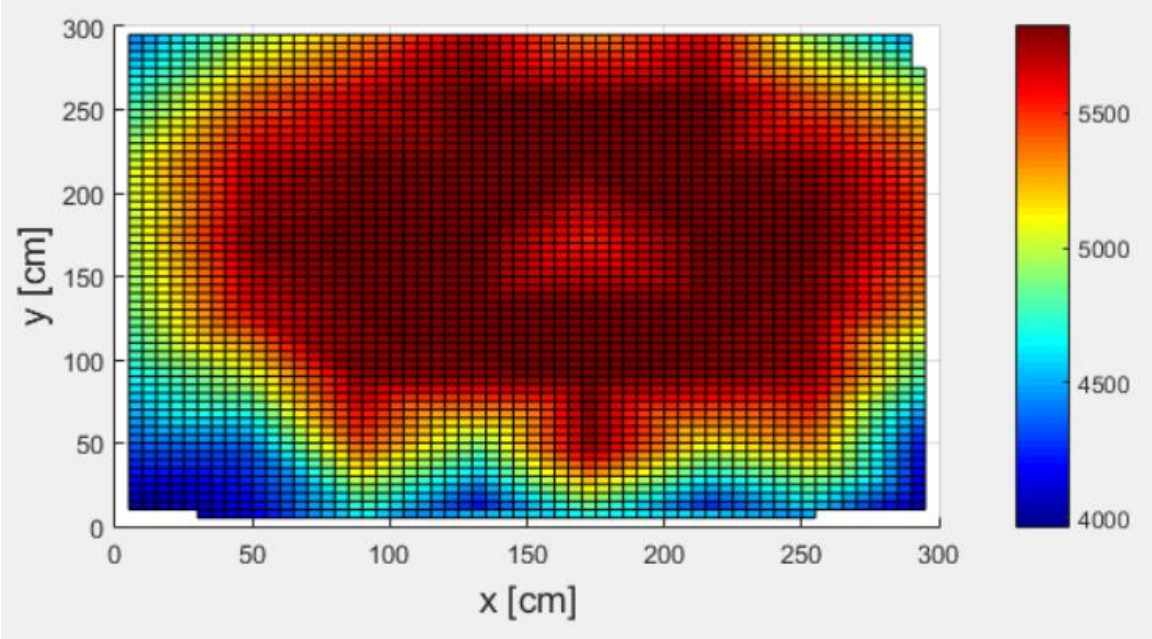

Figure 4.18: Open Room with 262 µCi Cs-137 Source Surface Plot for 16 µCi Threshold

The sides of the plateau show an improvement in resolution as the threshold is lowered. The lighter red section of Figure 4.22 is where the source was located. The slightly fewer counts is most likely due to the loss of a data packet during wireless transmission between the robot and the computer. The resolution of the cesium identification can be improved by focusing on the channels associated with the cesium source peaks, as seen in Figure 4.23**.**

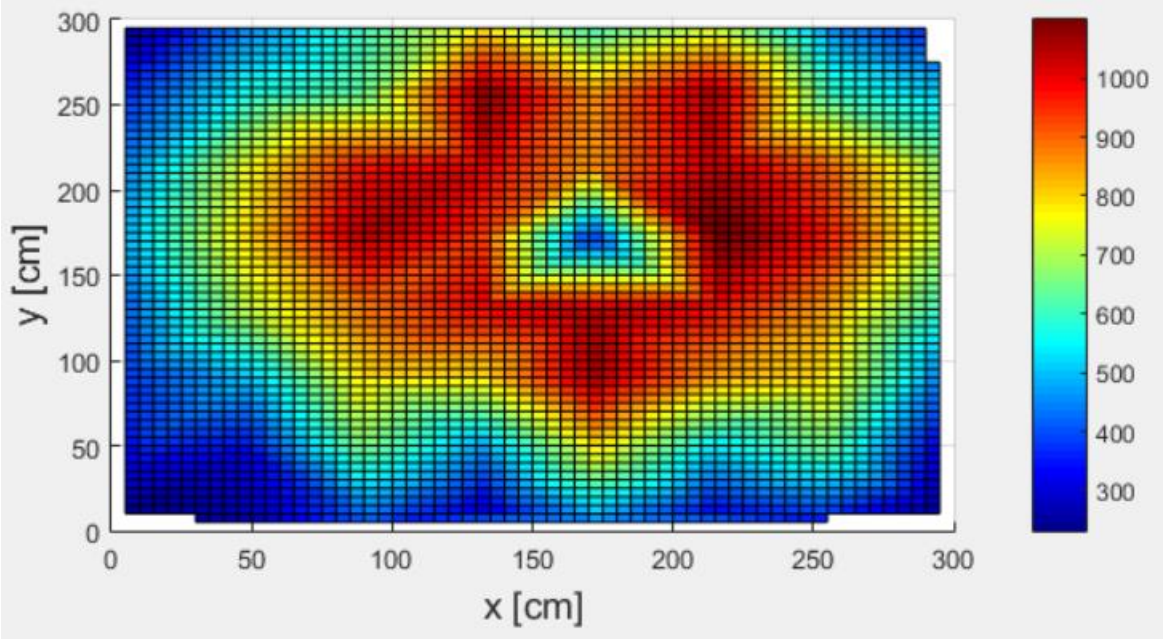

Figure 4.19: Cs-137 Peak Channels Surface Plot of 262 µCi Cs-137 Source for 16 µCi Threshold in Open Room

The source location is made very obvious due to the lack of counts. The reduction in counts was due to the oversaturation of the detector causing in a shift of the cesium peak to lower channel numbers. Although this can be advantageous in certain situations, this can also give false characterizations of sources and reduce the chance of other sources being discerned.

The co-robot was then released in the one-obstacle room scenario, and the results were compared to the zero-obstacle scenario. The 16 µCi threshold was used for the remainder of the runs, as it was deemed sufficiently accurate to capture the 1 µCi source while maintaining high resolution and reasonable speed. The comparable 100 µCi threshold runs can be found in Appendix B. Figure 4.24 shows the one-obstacle room with a 1 µCi cesium source located at the second position, and Figure 4.25 shows the path taken by the co-robot.

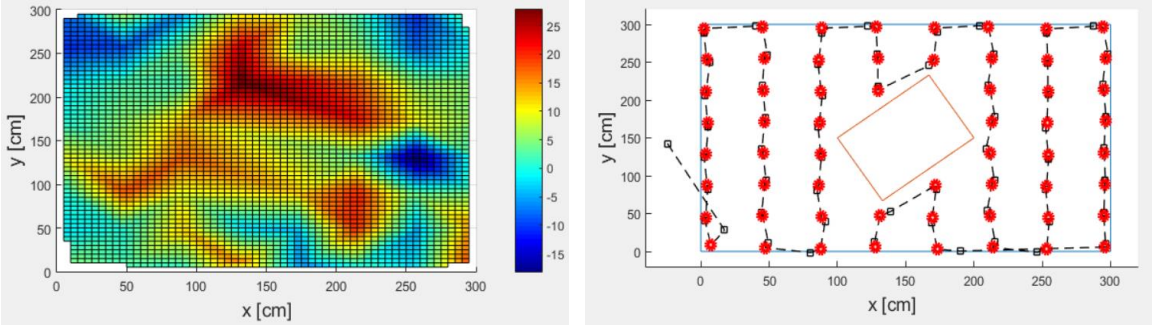

Figure 4.20: Left -- Cs-137 Peak Channels Surface Plot of 1 µCi Cs-137 Source for 16 µCi Threshold in One-Obstacle Room, Right -- Run Path of 1 µCi Cs-137 Source for 16 µCi Threshold in One-Obstacle Room

Although the co-robot was able to distinguish the 1 µCi source located within the obstacle, it proceeded to navigate to the northern tip of the obstacle. This was not the location closest to the source; however, it was the location of the highest cesium counts, as seen in Figure 4.24. This is not ideal, as it would require a longer run to be made with more survey locations, at which point the source may be too far within the obstacle boundaries to be accurately located. The larger cesium was easily found as seen in Figure 4.26 and used a similar path. The co-robot proceeded to approach the located source, and the resulting 2 minute spectrum count can be seen in Figure 4.27.

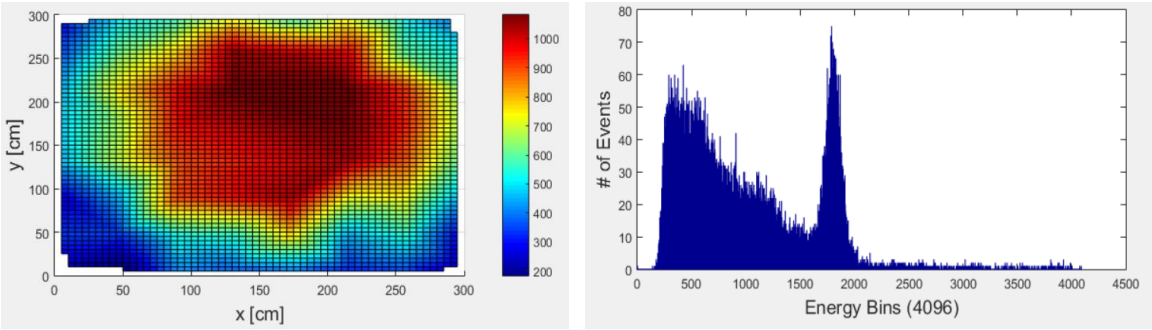

Figure 4.21: Left -- Cs-137 Peak Channels Surface Plot of 262 µCi Cs-137 Source for 16 µCi Threshold in One-Obstacle Room, Right -- Cs-137 Peak Channel Spectrum of 262 µCi Cs-137 Source for 16 µCi Threshold in One-Obstacle Room

The surface plot of Figure 4.26 shows a distinct area of high counts where the source was observed, but because the co-robot could not get close enough to the source, there is

no shift in the cesium peak in either figure. The same test was completed for the two-obstacle room with the third source location, and this case, the smaller cesium source was located properly as seen in Figure 4.28. The path did, however, cross through one of the obstacles as seen in Figure 4.29, and would need a waypoint adjustment if the obstacles were physically present.

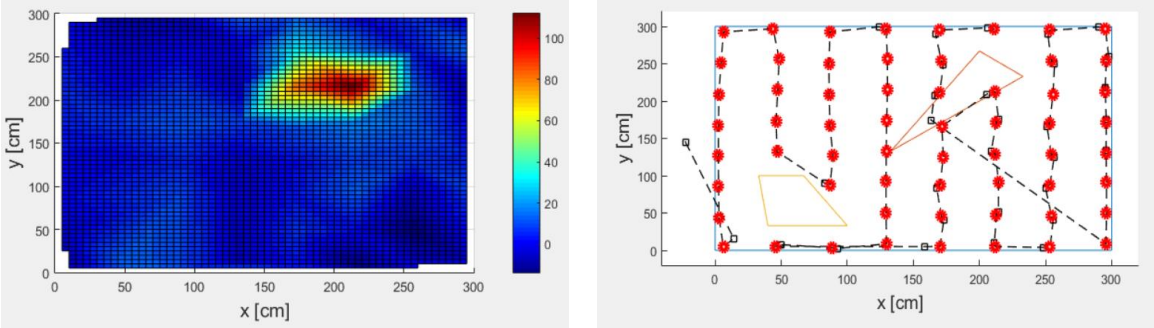

Figure 4.22: Left -- Cs-137 Peak Channels Surface Plot of 1 µCi Cs-137 Source for 16 µCi Threshold in Two-Obstacle Room, Right -- Run Path of 1 µCi Cs-137 Source for 16 µCi Threshold in Two-Obstacle Room

The next set of runs conducted were the high speed runs. The objective of these runs was to determine if the total count time of the co-robot could be significantly reduced. The two Cs sources were once again tested, and the 262 µCi source runs can be found in Appendix B. The tests using the 1 µCi Cs-137 source are depicted in Figures 4.30 and 4.31 for 5 and 2 seconds respectively, and were conducted in an open room configuration.

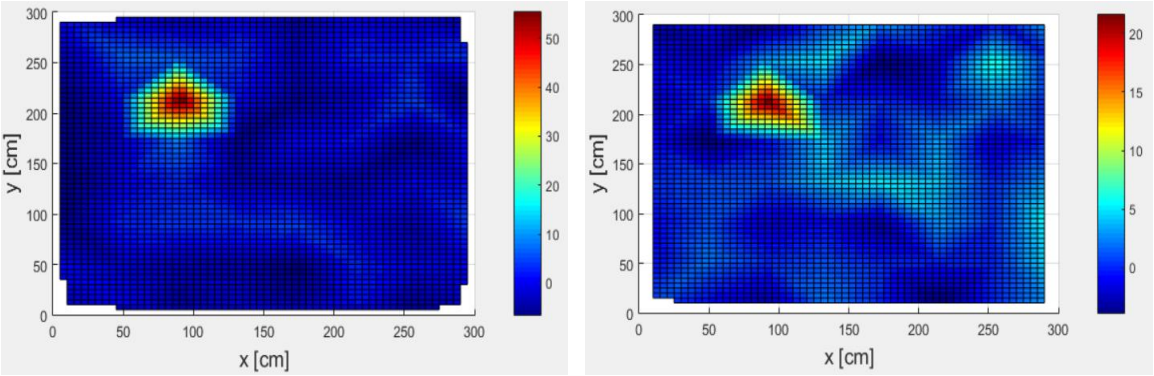

Figure 4.23: Cs-137 Peak Channels Surface Plot of 1 µCi Cs-137 Source for 16 µCi Threshold for 5 Sec Counts, Right -- Cs-137 Peak Channels Surface Plot of 1 µCi Cs-137 Source for 16 µCi Threshold for 2 Sec Counts

The results of both runs were more precise than predicted. The runs which were assigned 5 and 2 seconds per count took 17 minutes and 11 minutes to complete. This was a significant decrease in time, from the original 22 minutes needed for 10 second runs, and 28 mins needed for 15 second runs. As time is a crucial factor for multi-rotor vehicles, this is a very promising result for the potential application of the detection system to aerial vehicles.

The most significant advantage of gamma spectroscopy is the ability to characterize the sources based on the energy spectrum provided by the CsI detector. To determine the aptitude of the detection system for multiple sources, the open room configuration was used in conjunction with a variation of cobalt-60, sodium-22, and both cesium-137 sources. The runs were conducted using 10 second counts. The 1 and 262 µCi cesium sources were placed in both a close location and a far location from the 2 µCi cobalt and 1 µCi sodium in an attempt to distinguish between the two sources. The 1 uCi cesium source was placed at location 2 for all tests. Figures 4.32 and 4.33 show the effects of distance when the 2 uCi cobalt source location was varied between locations 1 and 3.

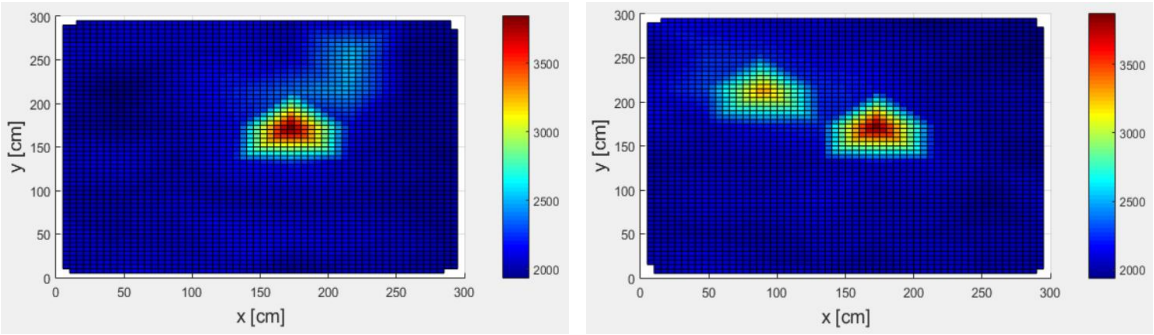

Figure 4.24: Left -- Cs-137 Source Location 2 and Co-60 Source Location 3 for 10 Sec Counts in Open Room with 16 µCi Threshold, Right -- Cs-137 Source Location 2 and Co-60 Source Location 1 for 10 Sec Counts in Open Room with 16 µCi Threshold

Although the cobalt was more noticeable in source location 1, Figures 4.34 and 4.35 show that the cobalt was distinctly observed in both instances, though at a lesser total count level than the cesium source.

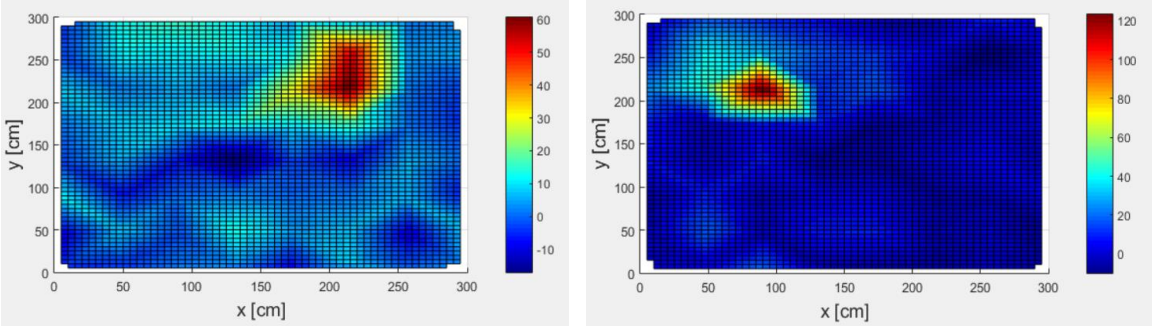

Figure 4.25: Left -- Co-60 Peak Channels Surface Plot Co-60 Source at Location 1 for 10 Sec Counts in Open Room with 16 µCi Threshold, Right -- Co-60 Peak Channels Surface Plot Co-60 Source at Location 3 for 10 Sec Counts in Open Room with 16 µCi Threshold

Na-22 was then added to the open room in location 2 while keeping the other parameters constant. Figure 4.36 displays the total counts observed during this run. Figure 4.37 displays the cesium spectrum surface plot and Figure 4.38 displays the sodium spectrum surface plot. I.e. Figure 4.37 shows the count distribution for channels 1700 to 1900, which are associated with Cs, and Figure 4.39 shows the count distribution for energies 3000 to 4000 associated with Co. There was some overlap between the energies of the different sources, as Na-22 has two energy peaks located at 511KeV and 1275KeV. The first is within 150KeV to cesium and the second is centered in the middle of the both cobalt-60 peaks. As a result, Figure 4.39**,** which displays the cobalt spectrum surface plot, also shows a part of the two sodium energy peaks.

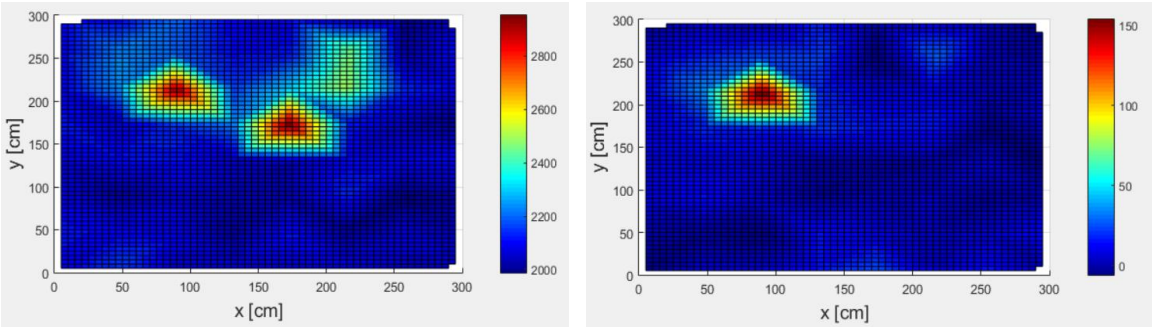

Figure 4.26: Left -- Surface Plot for Cs-137, Na-22, and Co-60 Source at Location 1, 2, and 3 for 10 Sec Counts in Open Room with 16 µCi Threshold, Right -- Cs-137 Peak Channels Surface Plot Cs-137 Source at Location 1 for 10 Sec Counts in Open Room with 16 µCi Threshold

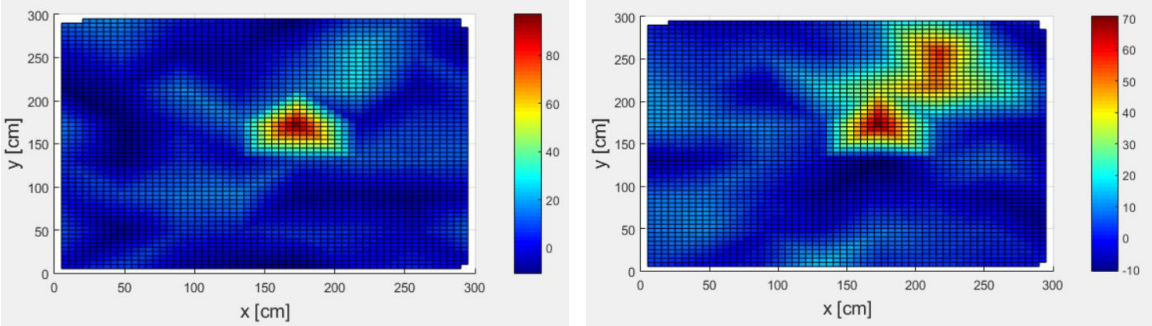

Figure 4.27: Left -- Na-22 Peak Channels Surface Plot Na-22 Source at Location 2 for 10 Sec Counts in Open Room with 16 µCi Threshold, Right -- Co-60 Peak Channels Surface Plot Co-60 and Na-22 Source at Location 3 and 2 for 10 Sec Counts in Open Room with 16 µCi Threshold

The cobalt signature that appears in Figure 4.38 was expected due to the Compton continuum. All three sources can be easily distinguished, but currently the co-robot only approaches the location where it observed the most activity. As a result the co-robot approached the Na-22 source, but in the future the algorithm would be expanded such that it approaches approach all distinct sources.

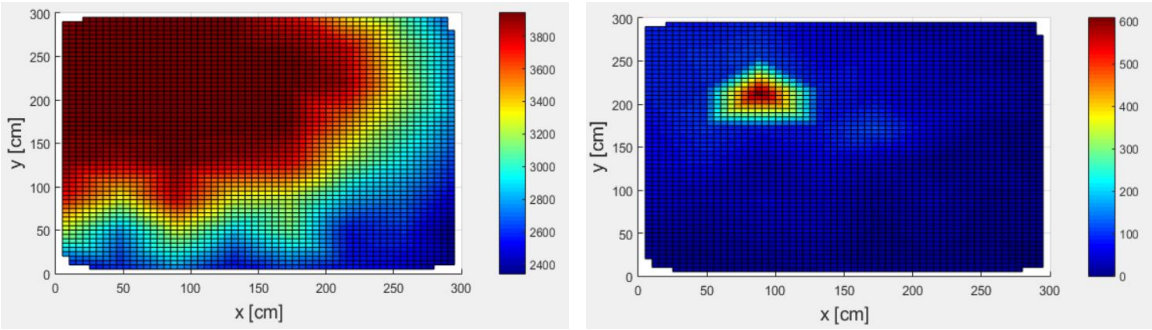

Figure 4.28: Left -- Surface Plot for Large Cs-137, Na-22, and Co-60 Source at Location 1, 2, and 3 for 10 Sec Counts in Open Room with 16 µCi Threshold, Right -- Na-22 Peak Channels Surface Plot for Large Cs-137 and Na-22 Source at Location 1 and 2 for 10 Sec Counts in Open Room with 16 µCi Threshold

When the large cesium source was placed into the room instead of its smaller counterpart, the source overshadowed the smaller sources on the total counts, as displayed in Figure 4.40. The results also highlighted the issue of the shifting peaks, as the sodium source was obscured by the shifted cesium peak seen in Figure 4.41**.** The cobalt spectrum

in **Figure 4.42**, however, reflected both the sodium and cobalt signatures, as would be expected.

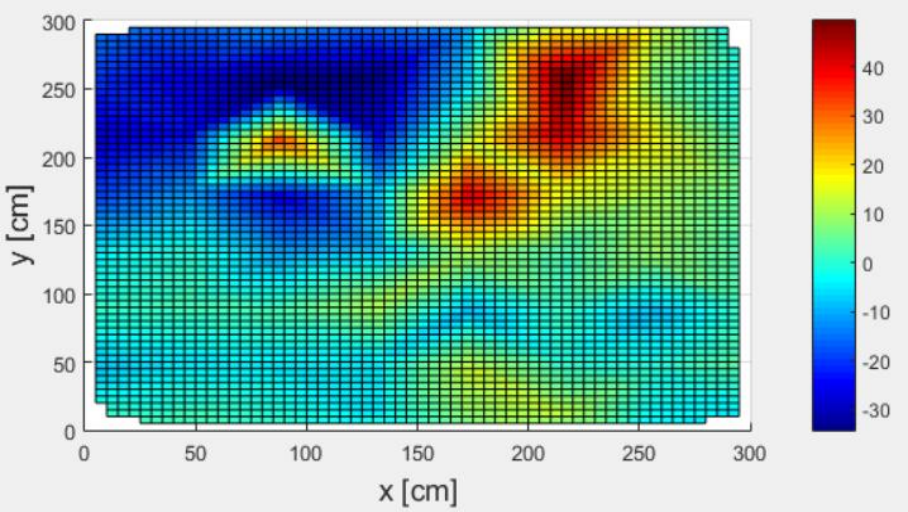

Figure 4.29: Co-60 Peak Channels Surface Plot for Large Cs-137, Na-22, and Co-60 Source at Location 2 and 3 for 10 Sec Counts in Open Room with 16 µCi Threshold

The most interesting experiment was to assess the co-robot's response to partially shielded sources. For this test, the large Cs-137 was used and shielded by lead on three sides. The fourth side was shielded by concrete as seen in Figure 4.45. The blocks were set in the middle of the center obstacle and the vehicle was run according to the single obstacle algorithm. The resulting path and photon flux are shown in Figure 4.43 and Figure 4.44.

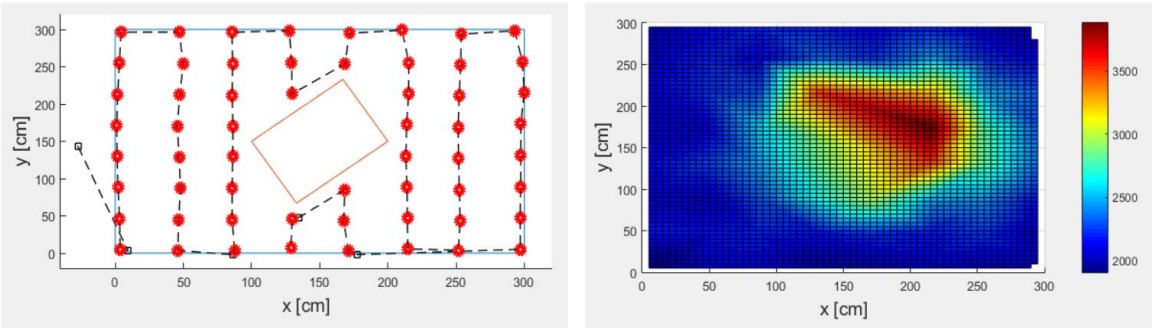

Figure 4.30: Left -- Path of Co-robot to Avoid Shielding with 16 µCi Threshold and 262 µCi Cs-137 Source, Right -- Surface Plot for a 262 µCi Cs-137 Source with Shielding at Center with 16 µCi Threshold

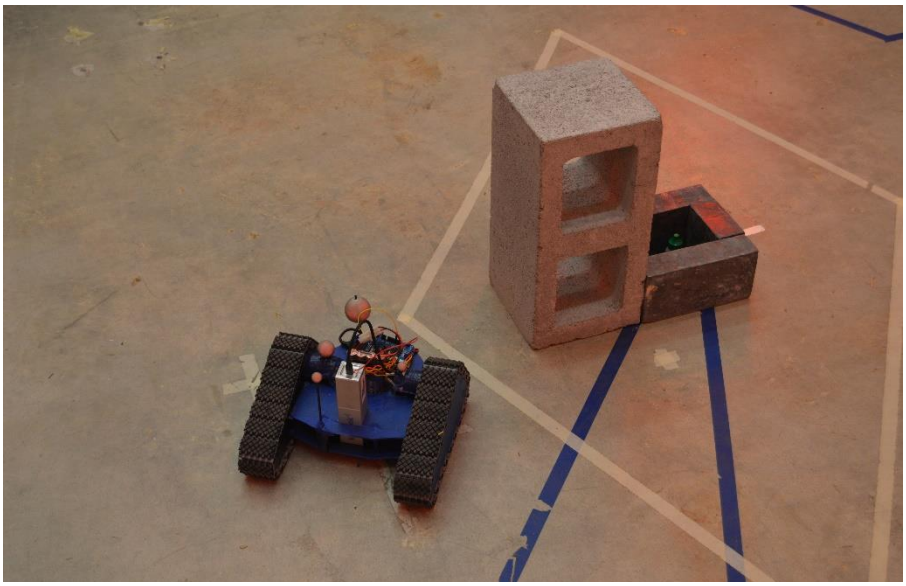

Figure 4.31: Shielding with Concrete and Lead Setup with Co-robot Final Position

Figure 4.45 also gives a comparison between the size of the middle obstacle and the size of the co-robot. Although there was a large reduction in counts, the detector was able to find the source and accurately characterize it. Given that many potential scenarios for this vehicle involve hard to locate sources, it is promising that these test were successful. There were two additional shielding configurations that were tested, and the results can be found in Appendix B.

The last test combined multiple aspects of previous tests. The larger cesium source was placed in the middle of the room with lead shielding on several sides as shown in Figure 4.46. The sodium and cobalt sources were then placed outside of the shielding walls, and outside of the beam lines of the cesium. The total spectrum, as well as the cesium, sodium, and cobalt spectrums are shown in Figures 4.47, 4.48, 4.49, and 4.50.

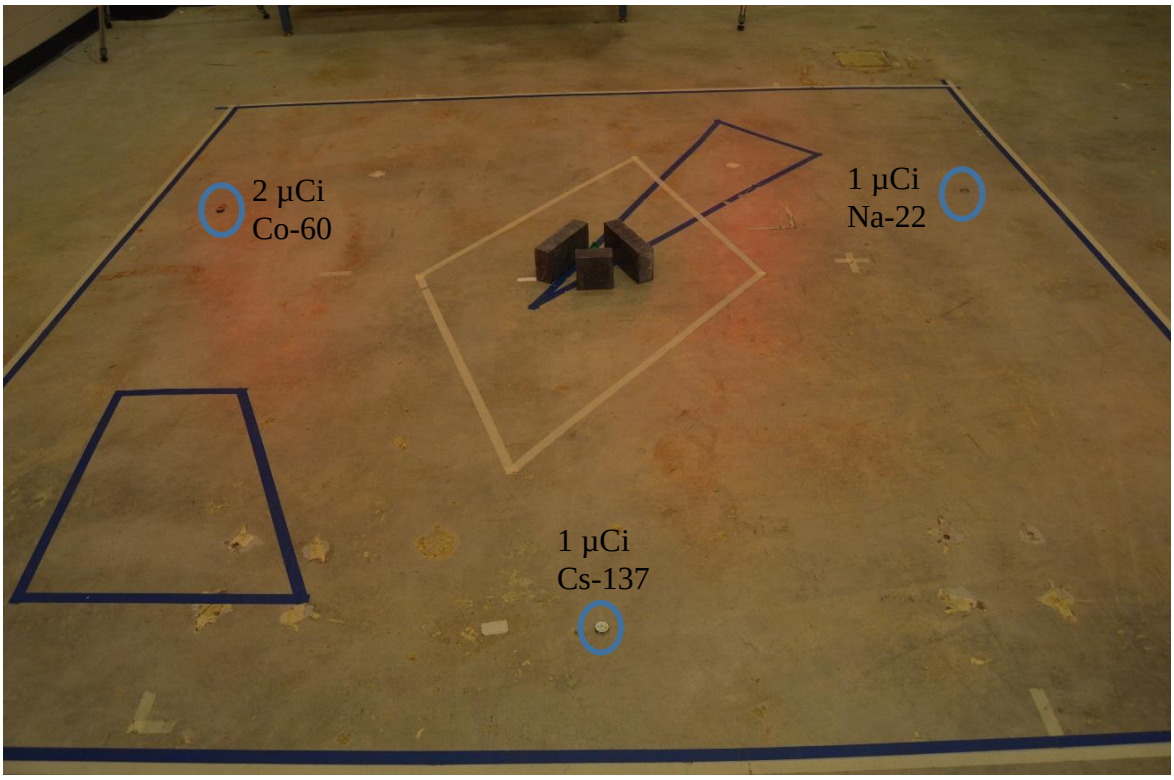

Figure 4.32: Setup with Shielding on Three Sides and 262 uCi Cs-137, 2 uCi Co-60, 1 uCi Na-22, and a 1 uCi Cs-137 Source.

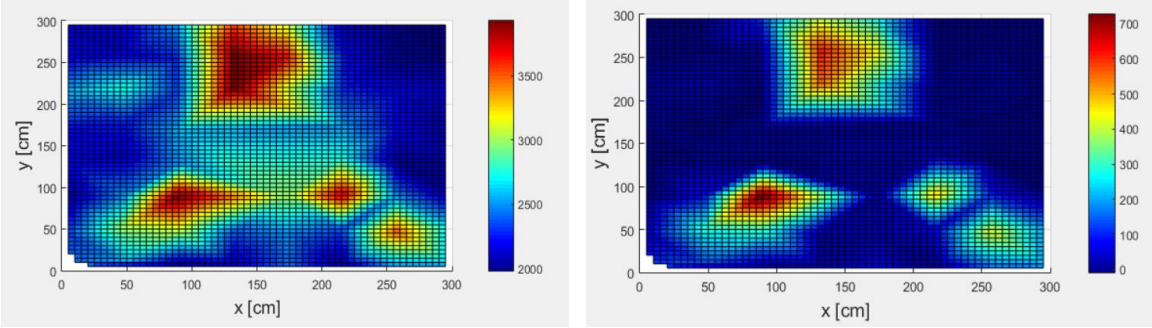

Figure 4.33: Left -- Surface Plot for 4 Sources with Triangle Shielding at Center with 16 µCi Threshold and 10 Sec Counts, Right -- Cs-137 Surface Plot for 4 Sources with Triangle Shielding at Center with 16 µCi Threshold and 10 Sec Counts

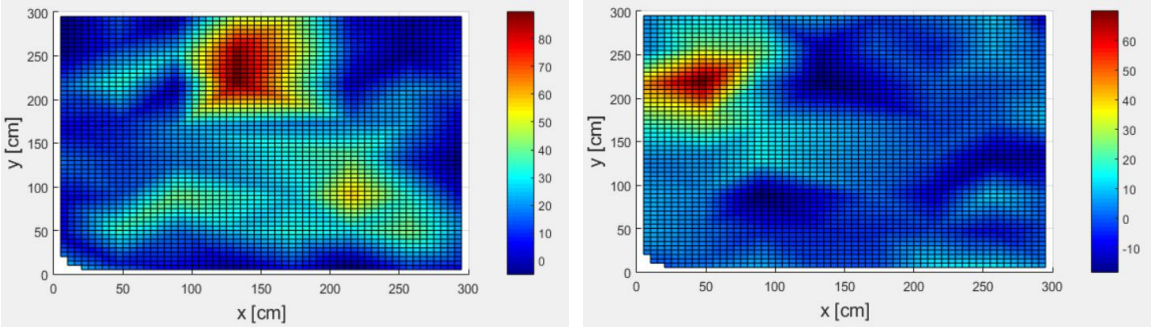

Figure 4.34: Left -- Na-22 Surface Plot for 4 Sources with Triangle Shielding at Center with 16 µCi Threshold and 10 Sec Counts, Right -- Co-60 Surface Plot for 4 Sources with Triangle Shielding at Center with 16 µCi Threshold and 10 Sec Counts

The resulting photon fluxes do not distinguish the sodium and smaller cesium sources precisely, but both the cobalt and larger cesium sources are immediately visible. The three exits on the shielding triangle also form recognizable beams that are easily characterized by the co-robot.

CHAPTER 5

CONCLUSION AND FUTURE WORK

5.1 Conclusion

There are a vast number of applications for automated co-robots in radiation mapping and non-proliferation uses. The use of co-robots, either terrestrial or aerial, can eliminate the health and safety risks of radiation exposure for workers in the event of an emergency situation. Recent events have highlighted the increasing need for safe methods of quick-response autonomous radiation detection, but the applications of co-robots extend far beyond the rare case of catastrophic failure. It can be implemented in everyday monitoring, as well as threat assessment in a time where security is increasingly prioritized. Human independent radiation detection is guaranteed to grow rapidly in parallel with the growth of robotic technology and experience, which will improve the ability to avoid the dangerous scenarios that arise in human-based radiation detection. The work outlined in this project is a concrete step towards autonomous radiation detection that resulted in working prototypes for both neutron and photon detection. Both of the detection systems outlined are compact and accurate, making them strong contenders for advanced co-robots such as aerial vehicles. The neutron setup was able to effectively locate the radiation source, but further work is necessary to thermalize the neutrons at the detector rather than at the source. The communication system for the B-10 detector was ideal due to the smaller quantities of data being transmitted. The vehicle used for the neutron detection was not suitable due to the inconsistent turn radius but the alternate found for the photon setup exceeded all expectations.

The gamma system and the co-robot algorithm demonstrated the capability to locate and characterize sources autonomously with more accuracy and precision than initially

expected. Although many restrictions of obstacles and complex scenarios can impede the co-robot, the performance in the test scenarios was remarkable. The most crucial improvement needed for the algorithm is a revised obstacle avoidance system that recognizes the travel between cells. However, the algorithm was able to consistently and precisely detect sources above, and often below, the set threshold. As a result, the thresholds permitted the creation of more efficient paths, reducing the total time needed to complete a test. The high speed runs also conclusively confirmed the ability of the co-robot to reduce count times at each location while maintaining high resolution of the radiation map. This introduces the possibility of continuous counting implemented during robot motion, which could be tested in future work.

The capability to characterize the individual sources was critical, and this goal was successfully achieved. Although the shifting peaks due to saturation of the detector make it more difficult to identify some sources, the most intense sources are readily identifiable. The resolution of the detector also improved the ease of spectrum differentiation when analyzing the source spectrums. A combination of the neutron and gamma detectors could further assist with the characterization, as well as improve the ability to locate shielded sources. The most significant limitation was that although the detector observed all the sources, it only completed the characterization of the most intense source. Thus it will be necessary in the future to develop the algorithm to approach all potential sources.

Most importantly, the current detection system can appropriately identify shielded sources, as well as complex multivariate configurations that would be encountered in real-world scenarios. Overall, both systems exceeded expectations, and this research has developed a platform for immense growth within future projects.

5.2 Future Work

Further development of these co-robots and detection systems would allow endless possibilities. The most beneficial advancements would be the addition of a GPS system, the reworking of the code to improve the object avoidance using an object-oriented coding language, and the upgrade of the on-board processor to support the combination of neutron and gamma detectors.

The greatest limiting factor of the current prototype is the need for the Vicon positional system. Although the system is ideal for testing and developing the algorithm due to its incredible precision, it is currently impossible for the co-robot to operate without it. A GPS system would give us the same information as the Vicon positional system in two and potentially three dimensions. Furthermore, the GPS would allow for the same tests to be conducted on a much larger scale, anywhere in the world.

The use of MATLAB for the algorithm coding has also posed challenges. It would be highly preferable to change the coding languages or restructuring the code to define the room and the obstacles. One method to do this would be to use an object-oriented coding language. The principal issue now is the dependence on the checkpoints to navigate the obstacles without intersecting any. Although the processing time of the code would likely be increased significantly, a shortest-path algorithm would be beneficial in order to reduce the run time once the object avoidance is improved.

Lastly, both the on-board processor and the radio frequency transmitter need to be upgraded. Currently the micro-processor is the sole limiting factor to the number of observed counts. A faster processor would allow for improved source localization, and reduce the chance of lost wireless data. A more robust processer would also allow the detector data to be partially processed on the board before being transmitted back to the main control station. This would allow for a significant reduction in the quantity of wireless transmissions. This would also support the combination of neutron and gamma detectors,

which should help locate and characterize sources even further. This project truly shows the future of radiation detection, and lays the foundation for infinite opportunities for improvements and specializations.

APPENDIX A

CODES

MCNP Code for Geometric Fraction

Calculate solid angle

c cells

1 0 10 -11 12 -13 14 -15 imp:n 1 $ inside rectangle

2 0 (-10:11:-12:13:-14:15) -2 imp:n 1 $ outside rectangle, inside boundary

3 0 2 imp:n 0 $ outside boundary

c surfaces

10 px -1.27

11 px 1.27

12 py 0

13 py 5.08

14 pz 10

15 pz 15

2 so 100

c data

sdef pos 0 0 0

f1:n 14

nps 1e9

APPENDIX B

ADDITIONAL RESULTS

100 µCi Threshold runs for one and two-obstacle room

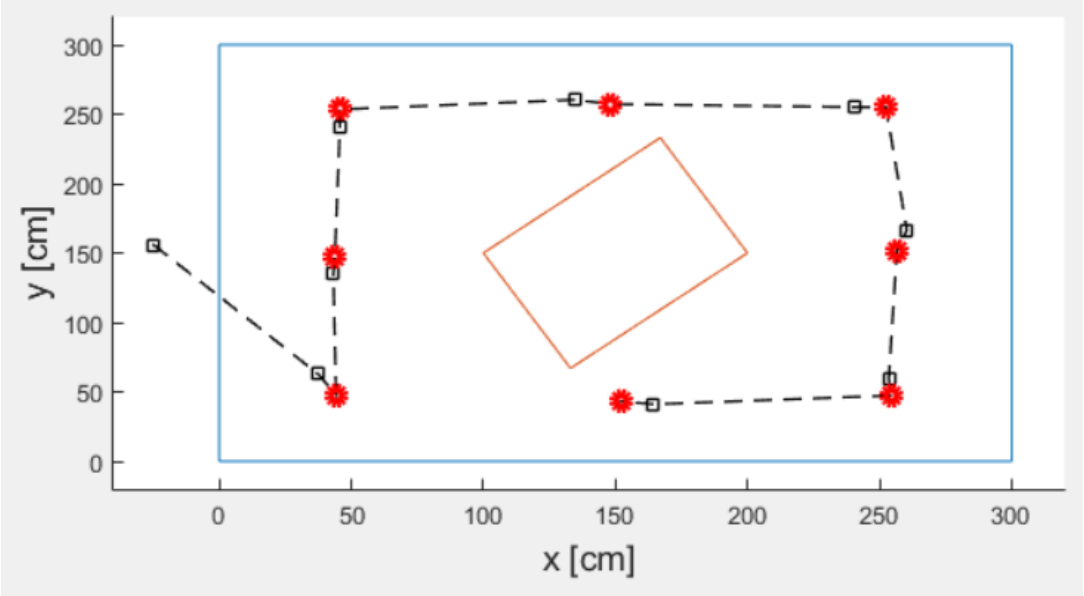

Figure B.1: Path of Co-Robot for One-Obstacle Room with 100 µCi Threshold

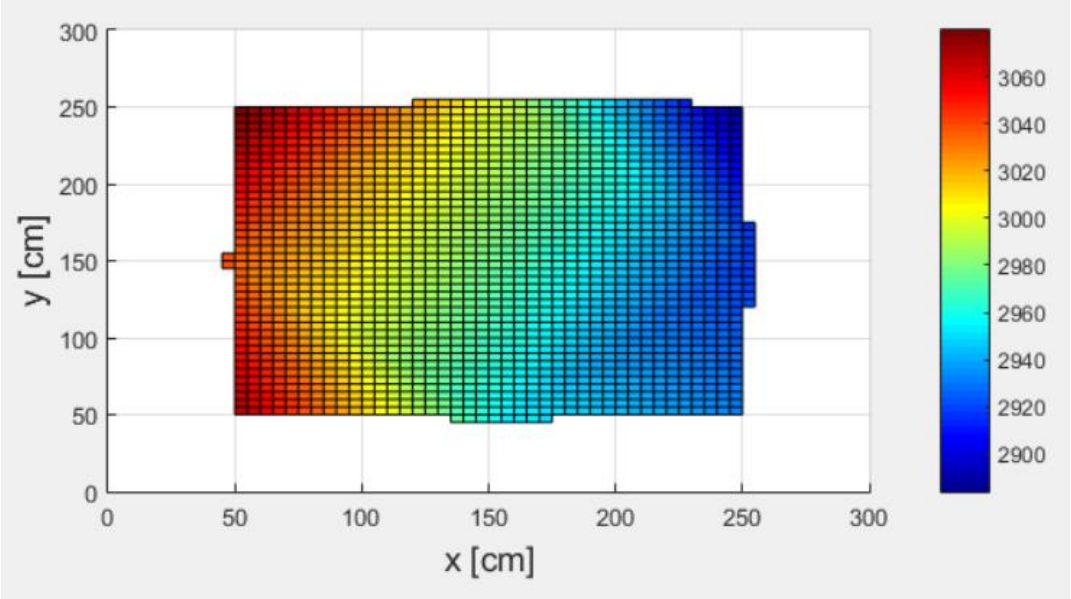

Figure B.2: Surface Map of Co-Robot for 1 µCi Cs-137 Source One-Obstacle Room with 100 µCi Threshold

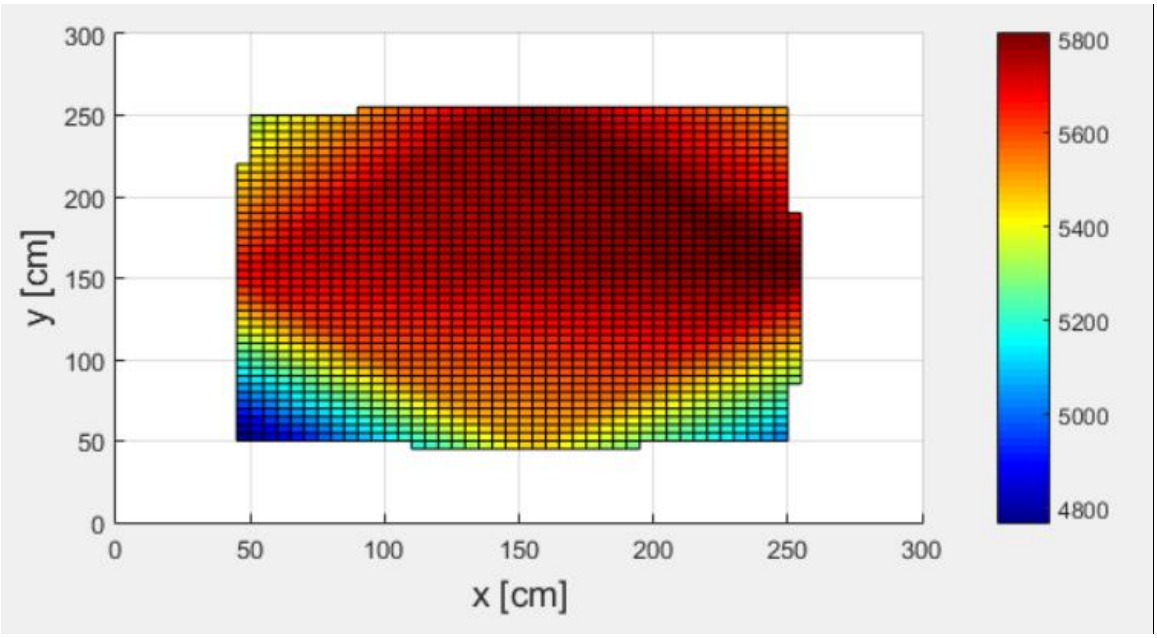

Figure B.3: Surface Map of Co-Robot for 262 µCi Cs-137 Source One-Obstacle Room with 100 µCi Threshold

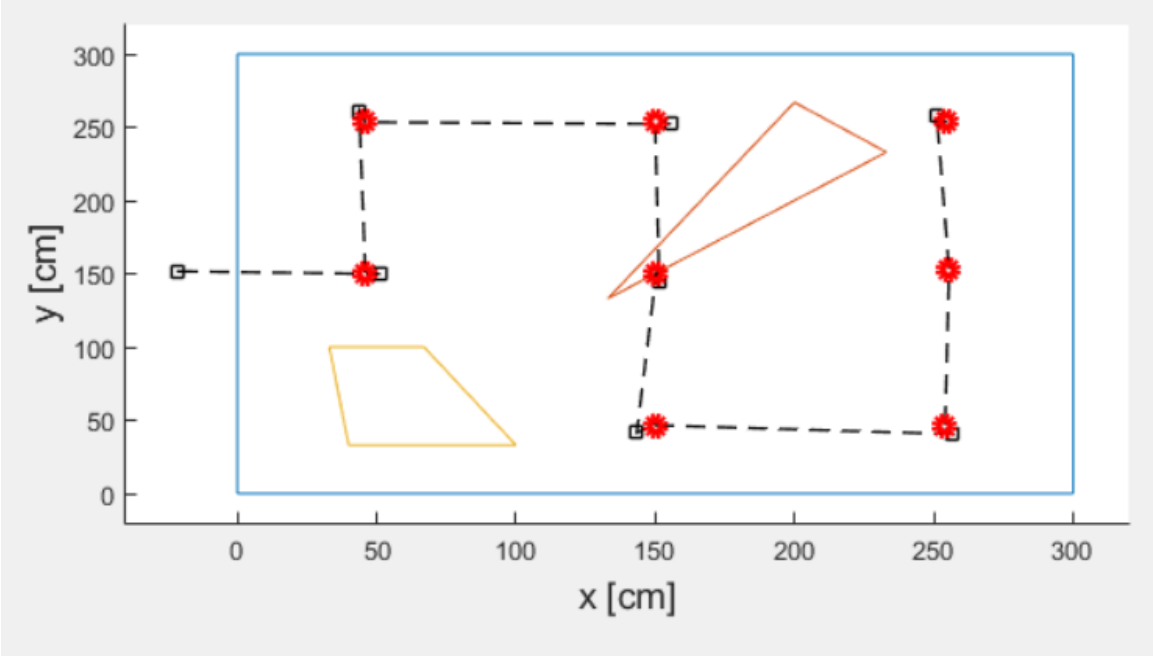

Figure B.4: Path of Co-Robot for Two-Obstacle Room with 100 µCi Threshold

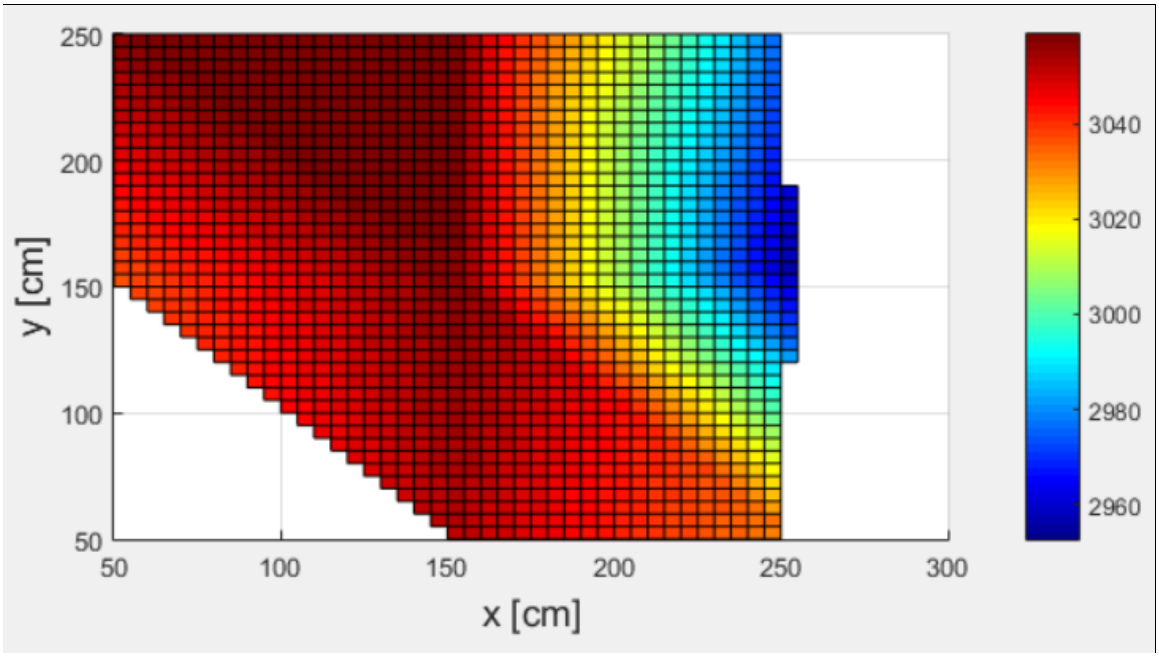

Figure B.5: Surface Map of Co-Robot for 1 µCi Cs-137 Source Two-Obstacle Room with 100 µCi Threshold

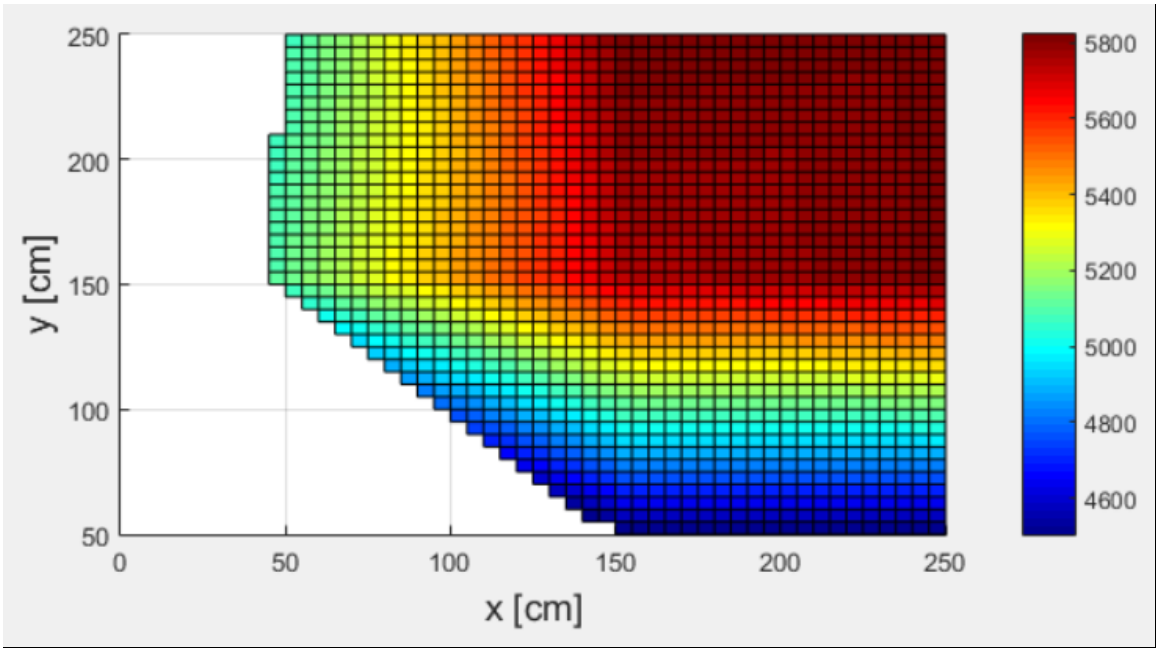

Figure B.6: Surface Map of Co-Robot for 1 µCi Cs-137 Source Two-Obstacle Room with 100 µCi Threshold

Large cesium source speed counting tests

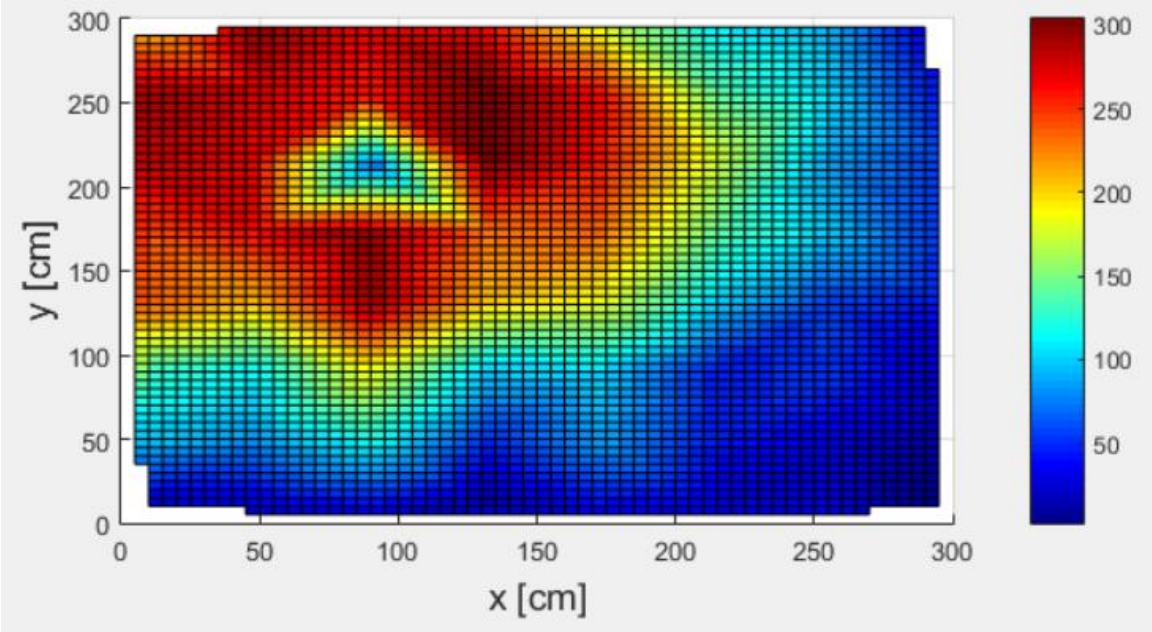

Figure B.7: Cs-137 Peak Channel Surface Plot for 262 µCi Source 5 Sec Speed Run with 16 µCi Threshold

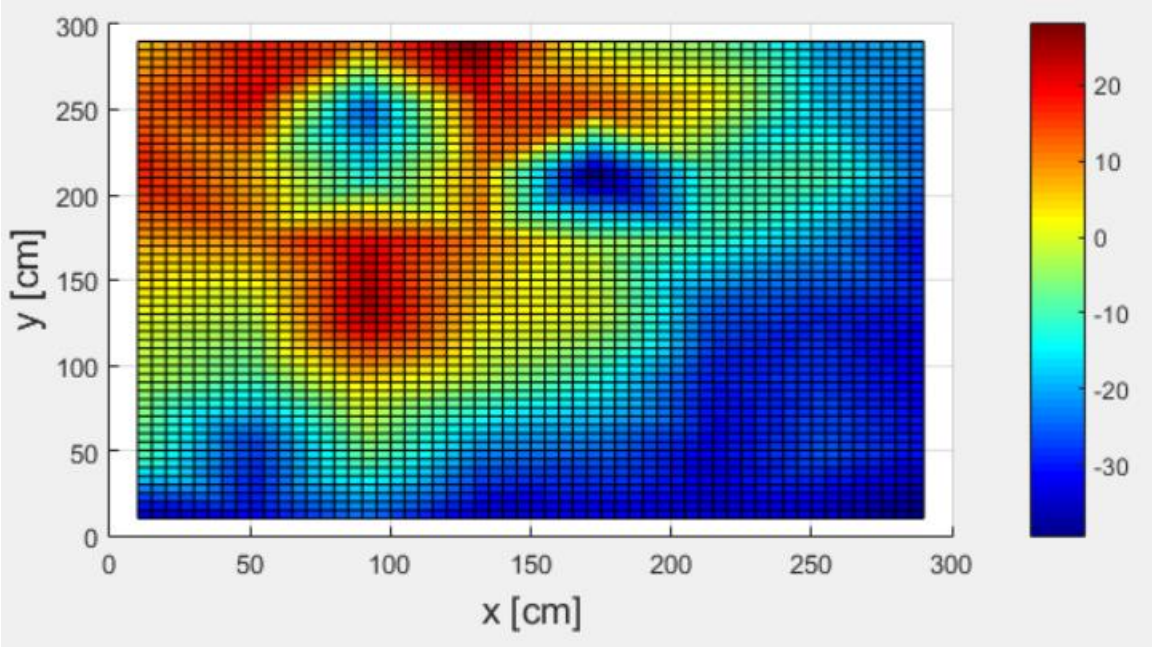

Figure B.8: Cs-137 Peak Channel Surface Plot for 262 µCi Source 2 Sec Speed Run with 16 µCi Threshold

Additional shielding runs

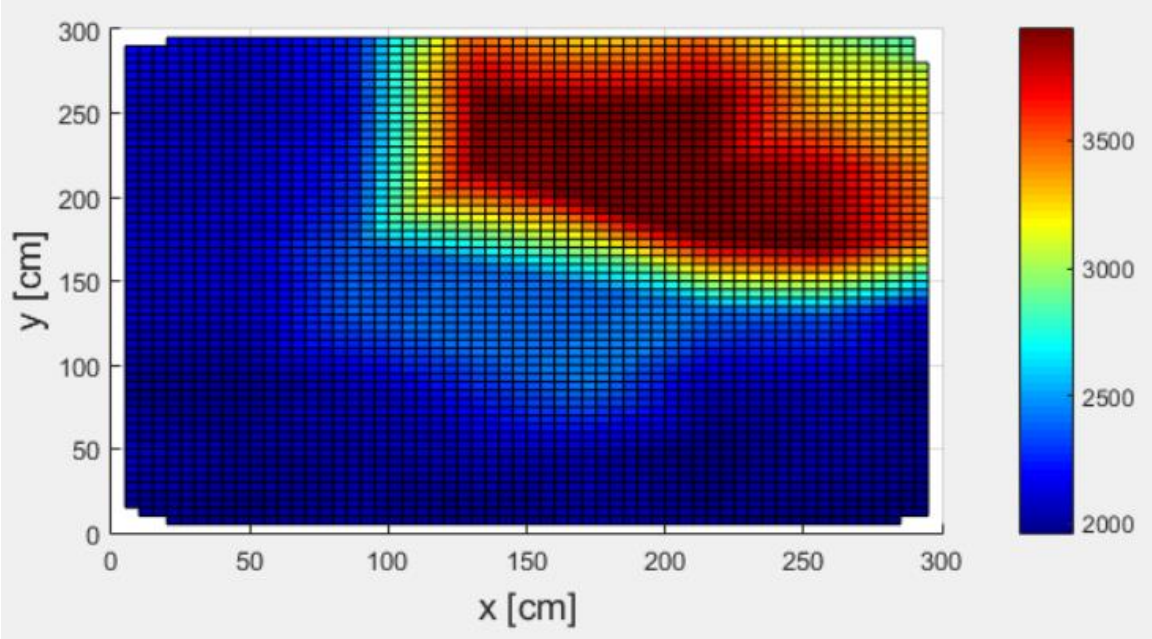

Figure B.9: Surface Map with Shielding on South and West of 262 µCi Cs-137 Source

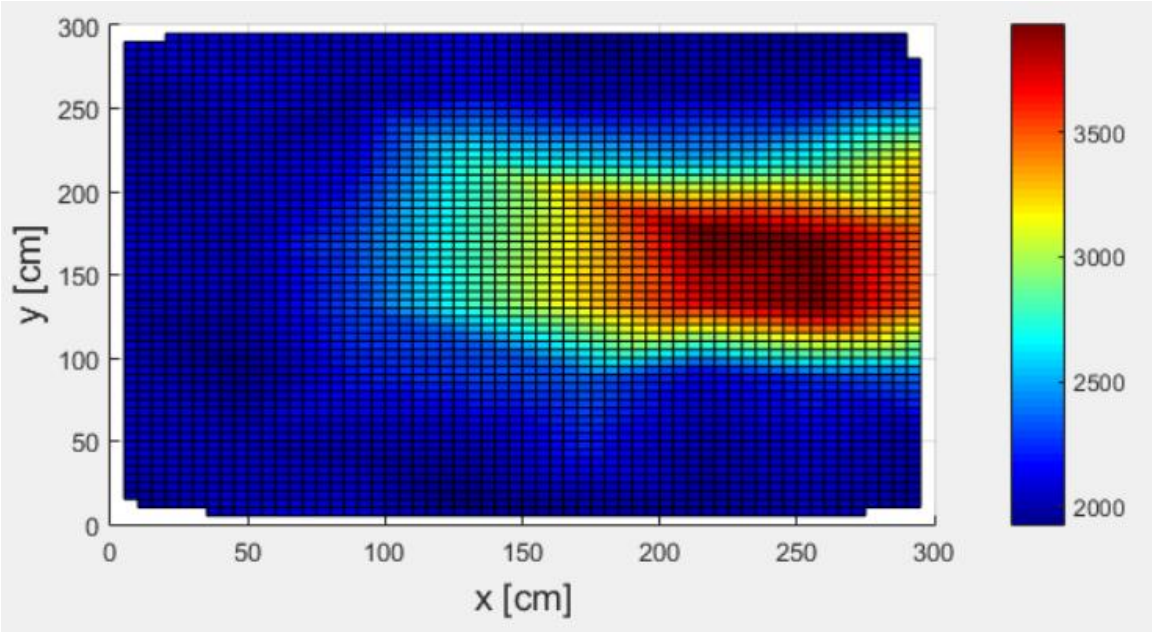

Figure B.10: Surface Map with Shielding on South, West, and North of 262 µCi Cs-137 Source

REFERENCES

[1] Choset, Howie, and Philipe Pignon. "Coverage Path Planning: The Boustrophedon Cellular Decomposition." Proc. of International Conference on Field and Service Robotics. N.p.: n.p., 1997. N. pag. Print.

[2] Cortez, R. A., X. Papageorgiou, H. G. Tanner, A. V. Klimenko, K. N. Borozdin, R. Lumia, and W. C. Priedhorsky. "Smart Radiation Sensor Management." *Robotics & Automation Magazine, IEEE* 15.3 (2008): 85-93. *IEEE Xplore*. Web. 6 Aug. 2015.

[3] Cortez, R. Andres, Herbert G. Tanner, and Ron Lumia. "Distributed Robotic Radiation Mapping." *ISER*. Proc. of Experimental Robotics, The Eleventh International Symposium, Greece, Athens. 2008 N.p.: n.p., n.d. N. pag. *ResearchGate*. Web. 7 Aug. 2015.

[4] Gonzalez-Banos, Hector H., and Jean-Claude Latombe. "Navigation Strategies for Exploring Indoor Enviornments." *The International Journal of Robotics Research* 11th ser. 21.10 (2002): 829-48. *Sage Journals*. Web. 7 Aug. 2015.

[5] Japan Nuclear Regulatory Authority. *Monitoring Air Dose Rates from a Series of Aircraft Surveys 30 Months After the Fukushima Daiichi NPS Accident*. Rep. Japan: NRA, 2013. Print.

[6] Knoll, Glenn F. *Radiation Detection and Measurement*. 3rd ed. New York: John Wiley & Sons, 2000. Print.

[7] Koren, Marina. "3 Robots That Braved Fukushima." *Popular Mechanics*. Hearst Digital Media, 09 Mar. 2012. Web. 6 Aug. 2015.

[8] Kromek. *Introducing Kromek's New Generation of Scintillator Products*. Durham, UK: Kromek, 2015. Print.

[9] Kumar, A., H. G. Tanner, A. V. Klimenko, K. Borozdin, and W. C. Priedhorsky. "Automated Sequential Search for Weak Radiation Sources." *IEEE Control and Automation* (2006): n. pag. *IEEE Explore*. Web. 7 Aug. 2015.

[10] Kurvinen, K., P. Smolander, R. Pollanen, S. Kuukankorpi, M. Kettunen, and J. Lyytinen. "Design of a Radiation Surveillance Unit for an Unmanned Aerial Vehicle." *Journal of Environment Radioactivity* 81 (2005): 1-10. *Science Direct*. Web. 6 Aug. 2015.

[11] Liu, Annie. *Simulation and Implementation of Distributed Sensor Network for Radiation Detection*. Thesis. California Institute of Technology, 2010. N.p.: n.p., n.d. Print.

[12] Martin, P. G., O. D. Payton, J. S. Fardoulis, D. A. Richards, and T. B. Scott. "The Use of Unmanned Aerial Systems for the Mapping of Legacy Uranium Mines." *Journal of Environment Radioactivity* 143 (2015): 135-40. *ScienceDirect*. Web. 10 Aug. 2015.

[13] MacFarlane, J. W., O. D. Payton, A. C. Keatley, G. P.T Scott, H. Pullin, R. A. Crane, M. Smilion, I. Popescu, V. Curlea, and T. B. Scott. "Lightweight Aerial Vehicles for Monitoring, Assessment and Mapping of Radiation Anomalies." *Journal of Environment Radioactivity* 136 (2014): 127-30. *ScienceDirect*. Web. 10 Aug. 2015.

[14] Mayhew, Christopher G., Ricardo G. Sanfelice, and Andrew R. Teel. "Robust Source-Seeking Hybrid Controllers for Autonomous Vehicles." *ACC*. Proc. of American Control Conference, NY, USA, New York. N.p.: IEEE, 2007. 1185-190. Print.

[15] Ministry of Education, Culture, Sports, Science and Technology (MEXT). *Results of Airborne Monitoring by the Ministry of Education, Culture, Sports, Science, and Technology and the U.S. Department of Energy*. Rep. 1st ed. N.p.: n.p., 2011. Print.

[16] Pang, Shuo, and Jay A. Farrell. "Chemical Plume Source Localization." *IEEE Transactions on Systems, Man, and Cybernetics* 36.5 (2006): 1068-080. *IEEE Explore*. Web. 6 Aug. 2015.

[17] Pollanen, Roy, Harri Toivonen, Kari Perajarvi, Tero Karhunen, Tarja Ilander, Jukka Lehtinen, Kimmo Rintala, Tuure Katajainen, Jarkko Niemela, and Marko Juusela. "Radiation Surveillance Using an Unmanned Aerial Vehicle." *Applied Radiation and Isotopes* 67 (2009): 340-44. *Science Direct*. Web. 6 Aug. 2015.

[18] Saint-Gobain. *CsI(Tl), CsI(Na) Cesium Iodide Scintillation Material*. N.p.: Saint-Gobain, n.d. *Http://www.crystals.saint-gobain.com/*. Saint-Gobain Ceramics & Plastics, Inc, June 2014.

[19] Saint-Gobain. *Efficiency Calculations for Selected Scintillators*. N.p.: Saint-Gobain, n.d. *Http://www.crystals.saint-gobain.com/*. Saint-Gobain Ceramics & Plastics, Inc., June 2014. Web.

[20] Sanada, Yukihisa, and Tatsuo Torii. "Aerial Radiation Monitoring Around the Fukushima Dai-ichi Nuclear Power Plant Using an Unmanned Helicopter." *Journal of Environment Radioactivity* 139 (2015): 294-99. *ScienceDirect*. Web. 10 Aug. 2015.

[21] Sanada, Yukihisa, Takeshi Sugita, Yukiyasu Nishizawa, Atsuya Kondo, and Tatsuo Torii. "The Aerial Radiation Monitoring in Japan after the Fukushima Daiichi Nuclear Power Plant Accident." *Progress in Nuclear Science and Technology* 4 (2014): 76-80. *Atomic Energy Society of Japan*. Web. 10 Aug. 2015.

[22] TEPCO. *Fukushima Nuclear Accident Analysis Report*. Tech. Tokyo Electric Power Company, 20 June 2012. Web.

[23] Valentine, John, William W. Moses, Stephen E. Derenzo, David K. Wehe, and Glenn F. Knoll. "Temperature Dependence of CsI(Tl) Gamma-Ray Scintillation Decay Time Constants and Emission Spectrum." *SPIE*. Proc. of International Society for Optics and Photonics, California, USA, San Diego. Vol. 1734. San Diego: n.p., 1992. 32-43. Print. Gamma-Ray Detectors.

[24] Wald, A. "Sequential Tests of Statistical Hypotheses." *The Annals of Mathematical Statistics* (1945): 117-86. *JSTOR [JSTOR]*. Web. 7 Aug. 2015.

[25] Zafrir, H., A. Pernick, G. Steinitz, U. Yaffe, and A. Grushka. "Unamanned Airborne System in Real-Time Radiological Monitoring." *Radiation Protection Dosimetry* 50.2-4 (1993): 295-99. *Oxford Journals*. Web. 6 Aug. 2015.